Title

Hindbrain modules differentially transform activity of single collicular neurons to coordinate movements.

Journal

Cell, 186(14)

Authors

Zahler, Sebastian
Taylor, David
Wright, Brennan
et al.

Publication Date

2023-07-06

DOI

10.1016/j.cell.2023.05.031

Peer reviewed

HHS Public Access

Author manuscript

Cell. Author manuscript; available in PMC 2024 July 06.

Published in final edited form as:

Cell. 2023 July 06; 186(14): 3062–3078.e20. doi:10.1016/j.cell.2023.05.031.

Hindbrain modules differentially transform activity of single collicular neurons to coordinate movements

Sebastian H. Zahler[1,2,†], **David E. Taylor**[1,2,†], **Brennan S. Wright**[1,2], **Joey Y. Wong**[1], **Varvara A. Shvareva**[1], **Yusol A. Park**[1], **Evan H. Feinberg**[1,2,3,4,*]

[1]Department of Anatomy, University of California San Francisco; San Francisco, CA, USA 94143.

[2]Neuroscience Graduate Program, University of California San Francisco; San Francisco, CA, USA 94143.

[3]Kavli Institute for Fundamental Neuroscience, University of California San Francisco; San Francisco, CA, USA 94143.

[4]Center for Integrative Neuroscience, University of California San Francisco, San Francisco, CA, USA 94143.

Summary

Seemingly simple behaviors such as swatting a mosquito or glancing at a signpost involve the precise coordination of multiple body parts. Neural control of coordinated movements is widely thought to entail transforming a desired overall displacement into displacements for each body part. Here we reveal a different logic implemented in the mouse gaze system. Stimulating superior colliculus (SC) elicits head movements with stereotyped displacements but eye movements with stereotyped endpoints. This is achieved by individual SC neurons whose branched axons innervate modules in medulla and pons that drive head movements with stereotyped displacements and eye movements with stereotyped endpoints, respectively. Thus, single neurons specify a mixture of endpoints and displacements for different body parts, not overall displacement, with displacements for different body parts computed at distinct anatomical stages. Our study establishes an approach

*Lead contact: evan.feinberg@ucsf.edu.
†These authors contributed equally.

Author contributions:
Conceptualization: S.H.Z., D.E.T, E.H.F.
Methodology: S.H.Z, D.E.T, B.S.W., E.H.F.
Software: S.H.Z, D.E.T, B.S.W.
Investigation: S.H.Z, D.E.T, B.S.W., J.Y.W., V.A.S, Y.A.P.
Formal analysis: S.H.Z, D.E.T, E.H.F.
Visualization: S.H.Z, D.E.T, E.H.F.
Writing – original draft: S.H.Z, D.E.T, E.H.F.
Writing – review & editing: S.H.Z, D.E.T, E.H.F.
Funding acquisition: E.H.F.
Project administration: E.H.F.
Supervision: E.H.F.

Declaration of interests: The authors declare no competing interests.

Inclusion and Diversity: We support inclusive, diverse, and equitable conduct of research. One or more of the authors of this paper self-identifies as a member of the LGBTQIA+ community.

for unraveling motor hierarchies and identifies a logic for coordinating movements and the resulting pose.

In Brief

Collicular projection neurons coordinate eye movement endpoint and head movement displacement by innervating specialized populations in pons and medulla, respectively.

Graphical Abstract

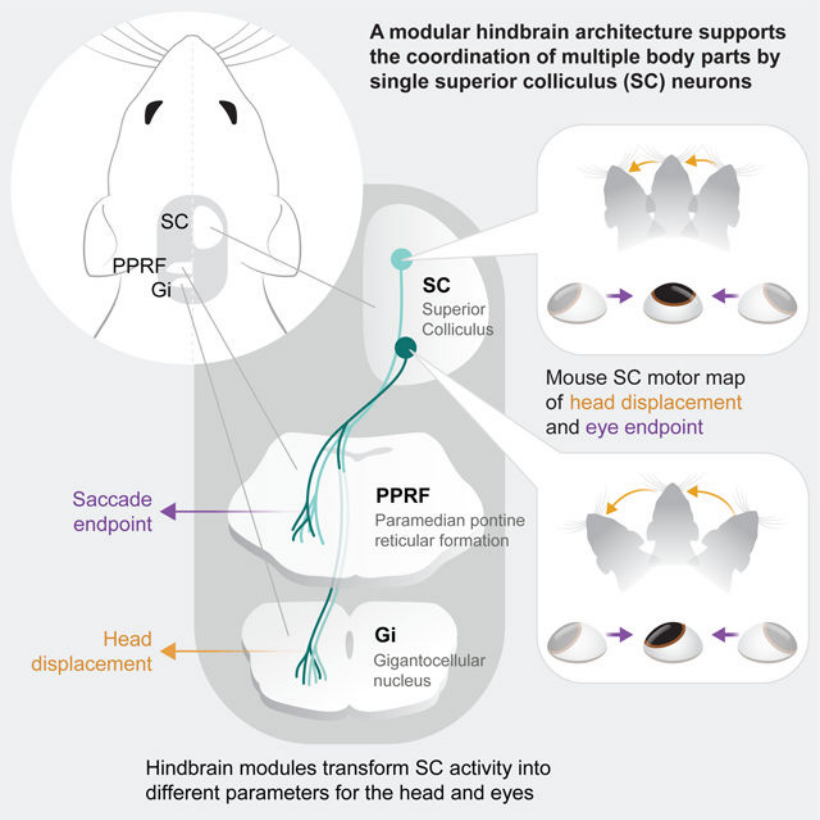

Introduction

Most behaviors involve moving multiple body parts. For example turning to identify the friend calling your name involves head and eye movements. Each body part has its own range of motion and can be positioned independently of the others. As a result, each body part may travel a different direction and distance (i.e., displacement) during a coordinated movement. How, then, does the brain determine the displacements for individual body parts during a coordinated movement?

It is widely believed that the brain achieves coordination through a hierarchical series of computations implemented within an anatomical hierarchy. In this view, neurons atop the hierarchy specify higher-level parameters such as the desired overall displacement, whereas neurons at lower levels decompose these higher-level parameters into displacements for each

body part[1–4]. Consistent with this model, stimulating brain areas or genetically defined cell types atop the anatomical hierarchy can evoke coordinated movements involving multiple body parts (e.g., grooming or bringing the hand to the mouth as though eating), whereas stimulating neurons at the bottom of the anatomical hierarchy can evoke stereotyped displacements of a particular body part[5–13]. However, little is known about where and how these hierarchical computations are instantiated within anatomical hierarchies[14–16]. In addition, these hierarchical frameworks have been studied primarily in the context of volitional behaviors such as trained reaching, but animals coordinate multiple body parts during innate, reflexive behaviors such as grooming, gaze shifts, avoidance, foraging, and escape as well[11,17–22]. Whether the computations hypothesized to underlie volitional behaviors apply to all coordinated movements is unknown.

Resolving how motor hierarchies in the brain transform higher-order movement plans into specific commands for individual body parts will require a stepwise, systematic interrogation of these circuits. Many studies have postulated that upper motor neurons in regions such as motor cortex and superior colliculus (SC) are key players in this process. Upper motor neurons connect higher centers to controllers in brainstem and spinal cord, and the axons of single upper motor neurons often collateralize to multiple areas[13,19,31–34,23–30]. These anatomical data suggest a mechanism whereby individual upper motor neurons carry signals used to coordinate multiple body parts[23]. For example, in the gaze system, it is widely believed that the higher-order parameter specified by upper motor neurons in SC is overall displacement (i.e., the sum of how far the head and eyes move)[35–38]. It is debated, however, where and how the desired overall displacement transforms into component head and eye displacements[35,37,38].

Here, we dissect the motor hierarchy controlling gaze shifts in the mouse. Our initial experiments unexpectedly revealed that mouse SC upper motor neurons do not specify the overall gaze displacement. Instead, their activity specifies the displacement for the head but only the endpoint for the eyes. In this sense, SC neurons multiplex displacements and endpoints for different body parts. Single SC upper motor neurons innervate two separate hindbrain populations that drive head movements with fixed displacements and eye movements with fixed endpoints, respectively. Neural recordings showed that head displacement information emerges in SC, whereas saccade information does not emerge until the hindbrain. Our study thus reveals that overall displacements are not computed at any anatomical stage within the mouse gaze hierarchy, and that displacements for different body parts are computed independently and at distinct anatomical stages, thereby uncovering unexpected diversity in mechanisms of coordinated movements.

Results

Mouse SC specifies head displacement and saccade endpoint but not overall gaze displacement

Superior colliculus (SC) controls orienting head and eye movements in a wide range of species, and stimulating SC elicits head and eye movements resembling those observed during sensory-guided gaze shifts[19,31,39–41]. We investigated head and eye movements driven by optogenetic stimulation of right SC in freely moving animals, focusing on the

horizontal axis, in which movements were largest (Figure 1A–C, Figure S1A–E)[42–45]. In primates and cats, it is believed that SC issues a gaze displacement command because stimulation of a single site elicits the same overall gaze displacement regardless of initial gaze direction[38]. To determine whether this is the case in mice, we examined the relationship between initial gaze direction and SC-evoked gaze displacement. Unexpectedly, SC stimulation evoked gaze shifts whose displacements depended on initial gaze direction (Figure 1D, E, H, I). Gaze displacement showed no dependence on initial head position but a strong dependence on initial eye position (Figure 1F–I). Together, these data suggest that mouse SC does not issue a fixed gaze displacement command.

We examined the head and eye components of SC-evoked movements to determine the basis for the eye position-dependence of gaze displacements (Figure 1J–U). Consistent with a previous report, right SC-evoked head movements had stereotyped displacements, i.e. leftward (contraversive) head movements that showed little dependence on initial head-body angle or the initial orbital positions of the eyes (Figure 1J, L, N, O)[31]. Moreover, head displacements were nearly invariant to the initial orbital positions of the eyes (Figure 1J–O, Figure S1J, K). In contrast, the rapid eye movements (saccades) evoked by SC stimulation displayed highly variable displacements but stereotyped endpoints (Figure 1P). This unexpected variability in saccade displacements was largely explained by initial eye position relative to the saccade endpoint (Figure 1S–U, Figure 1SJ, K). Interestingly, saccade probability showed a similar dependence on initial eye position such that saccades were likeliest when the eyes began far from the endpoint (Figure S1F, L, M). In contrast, initial head-body angle had little impact on saccade displacement (Figure 1R, T, U; Figure S1G). Thus, mouse SC drives head movements with stereotyped displacements and saccades with stereotyped endpoints, such that SC-evoked gaze displacement varies according to the initial position of the eyes.

To determine whether the stereotyped saccade endpoints observed during SC stimulation were due to the mechanical properties of the mouse oculomotor system, e.g., the elasticity of the extraocular muscles, we activated abducens motor neurons, which innervate the muscle that rotates the eye away from center (Figure S1N, O)[46,47]. Abducens stimulation caused movements of the ipsilateral eye with stereotyped displacements invariant to initial eye position, indicating that the effects of SC stimulation cannot be explained by the mechanical properties of the eye (Figure S1P–U).

Mouse SC comprises topographic maps of head displacement and saccade endpoint—Previous studies in mice demonstrated that SC-evoked head and eye movements depend on the site of stimulation within SC[31,48]. However, these studies did not examine the effects of initial eye position and therefore could not determine what movement parameters were represented topographically within this map. To facilitate comparisons with existing literature and to isolate SC-mediated eye movements from compensatory eye movements resulting from the vestibular ocular reflex (VOR), we performed electrical microstimulation at different sites within SC of head-fixed mice while monitoring the eyes and attempted head rotations (Figure 2A, Figure S2A, B)[41,42,48].

Consistent with previous studies, stimulating right SC evoked exclusively leftward (contraversive) attempted head movements that were larger for more posterior stimulation sites (Figure 2B, D, Figure S2G–H) (head displacement, shanks 1–4: −0.98 ± 0.42 Z, −1.42 ± 0.39 Z, −1.86 ± 0.39 Z, −2.20 ± 0.43 Z [mean ± s.d.]; $R^2 = 0.56$, $p < 10^{-6}$, n = 9 mice, linear regression). In addition, attempted head displacements were invariant to initial eye position, consistent with our findings in freely moving animals (Figure 2G, Figure S2C, D). In contrast to head movements, saccade displacements did not depend on the site of stimulation (Figure 2C, 2E) (saccade displacements, shanks 1–4: −6.9 ± 3.3°, −7.1 ± 2.1°, −8.4 ± 2.2°, −8.2 ± 2.3° [mean ± s.d.]; $R^2 = 0.05$, p = 0.18, n = 9 mice, linear regression). Strikingly, however, saccade endpoints depended on the site of stimulation, becoming more contralateral for more posterior stimulation sites (saccade endpoints, shanks 1–4: −1.8 ± 2.0°, −3.1 ± 2.0°, −5.6 ± 1.7°, −6.0 ± 2.7° [mean ± s.d.]; $R^2 = 0.37$, $p < 10^{-4}$, n = 9 mice, linear regression) (Figure 2C, F). As in freely moving mice, saccade endpoints were more stereotyped because of the strong dependence of saccade displacement and probability on initial eye position (Figure 2G, H, Figure S2E–J).

To more directly test the hypothesis that SC specifies saccade endpoints rather than displacements, we trained multinomial logistic regression classifiers to ask whether the site of stimulation in SC is better predicted by saccade displacements or endpoints (Figure 2I, J). Classifier performance using saccade endpoints was well above chance (0.37 ± 0.08 vs. 0.25; p = 0.005, n = 9 mice, one-sample Student's t-test), whereas classifier performance using saccade displacements was not significantly better than chance (0.26 ± 0.03 vs. 0.25; p = 0.09, n = 9 mice, one-sample Student's t-test) and significantly worse than performance using saccade endpoint (p = 0.004, two-sample Student's t-test). Together, these data indicate that mouse SC contains superimposed maps of head displacements and saccade endpoints, not overall gaze displacement.

Tectoreticular neurons specify head displacement and saccade endpoint—We next sought to identify the SC cells that drive these coordinated movements. Previous studies implicated SC upper motor neurons known as tectoreticular neurons in both head and eye movements, and bulk-labeled tectoreticular axons innervate multiple target sites in the contralateral ponto-medullary reticular formation (PMRF)[19,31,33,49]. To determine whether tectoreticular neurons drive coordinated head and eye movements in mice, we optogenetically stimulated SC axons in proximal contralateral PMRF of head-fixed mice, reasoning that because ChR2-mediated excitation drives both axon terminals and fibers of passage, this would excite axons arborizing within proximal PMRF as well as axons targeting more distal areas (Figure 3A)[50,51]. Indeed, stimulation of tectoreticular axons in PMRF evoked head and eye movements resembling those evoked by pan-neuronal SC stimulation (Figure 3B–G, Figure 2B, C). This suggested that tectoreticular populations drive head and eye movements with stereotyped displacements and endpoints, respectively.

To determine whether tectoreticular neurons are necessary for coordinated head and eye movements, we inhibited these neurons during an innate behavior wherein tactile stimuli elicit coupled saccades and attempted head movements closely resembling those elicited by SC stimulation (Figure 3H–N, Figure 1, Figure 2, Figure 3A–G)[41]. Consistent with our prediction, inhibiting tectoreticular neurons shifted whisker airpuff-evoked movements

rightward (ipsiversively) for both saccades and attempted head movements (Figure 3P, Q). Together, these optogenetic gain- and loss-of-function experiments demonstrate that mouse tectoreticular neurons drive gaze shifts by specifying head displacements and saccade endpoints.

Tectoreticular neurons encode stimulus location and head displacement— Next, we sought to understand how tectoreticular neurons encode eye and head movement commands during touch-evoked eye and attempted head movements. We performed extracellular electrophysiology in the deep layers of right SC, identifying ("optotagging") tectoreticular neurons as those antidromically activated by photostimulating SC axons in left (contralateral) PMRF (Figure 4A, B, Figure S3A, I–N)[52,53]. We first examined responses to airpuff stimulation of the whiskers (Figure 4C). We used whisker airpuffs because they uncouple head and eye movement directions (whisker airpuffs elicit attempted head movements predominantly towards the side of the stimulated whiskers but a nearly even mix of saccade directions) (Figure 3I–L). Tectoreticular responses to airpuffs exhibited two peaks resembling responses previously observed in mouse SC that are thought to reflect bottom-up input from trigeminal and top-down input from somatosensory cortex, respectively (Figure 4C, D Figure S3B)[54]. Most neurons were bilaterally responsive but nearly all with significant tuning preferred left (contralateral) (35/53) rather than right (ipsilateral) whisker airpuffs (1/53) (Figure 4D–E).

Next, we examined motor activity of tectoreticular neurons in SC. Previous studies in mice identified SC neurons tuned for specific head displacements[31]. We performed similar analyses, regressing attempted head displacement against spiking activity for each neuron (Figure 4G). Consistent with earlier studies, most right tectoreticular neurons preferred leftward (contraversive) attempted head movements (27/53), whereas no neurons preferred rightward (ipsiversive) attempted head movements (Figure 4H, Figure S3C)[31]. To control for correlation between airpuff location and attempted head movement direction, we examined attempted head movement tuning for a single airpuff location and observed similar results, albeit with fewer significantly tuned neurons because the decreased number of trials reduced the power of the statistical analyses (Figure S4A–C). Next, we examined tuning for saccade parameters. For each neuron, we regressed saccade displacement or endpoint location against spiking activity (Figure 4J, K, M, N). Few tectoreticular neurons showed tuning for saccade displacement (4/53) or saccade endpoint (5/53), and this small population of tuned neurons showed no overall bias for leftward versus rightward saccade displacements ($p = 0.63$, binomial test) or saccade endpoints to the left or the right of the median ($p = 1$, binomial test) (Figure 3K, N; Figure S3D, E). Finally, we repeated these analyses when trial data were aligned to movement onset rather than stimulus onset and analyzed non-optotagged SC units and observed similar results (Figure S3F–H, Figure S4D, E). These analyses also found only subtle differences in the laminar distribution of tuned cells in intermediate and deep SC (Figure S4F–J).

To examine neural population dynamics, we performed targeted dimensionality reduction on tectoreticular responses pooled across experiments. For each sensory or motor variable, we estimated a coding dimension (CD) that best separated left and right trials and projected population activity onto these dimensions. Consistent with our tuning analyses, population

activity was well-separated for whisker airpuffs and attempted head movements (Figure 4F, I). In contrast, there was no separation in population activity for saccade displacements or endpoints (Figure 4L, O). Together, these data demonstrate that tectoreticular neurons encode stimulus location and attempted head displacement, but not saccade displacement or endpoint, suggesting that saccade tuning emerges downstream of SC.

Distinct brainstem modules drive head movements with stereotyped displacements and saccades with stereotyped endpoints—Activating tectoreticular neurons drives head movements with stereotyped displacements and saccades with stereotyped endpoints, yet we found no evidence that the tectoreticular population encodes saccade parameters. This suggested that SC specifies head displacement whereas saccade endpoint and displacement are computed downstream. To better understand the role of downstream neurons in transforming tectoreticular activity into head and eye movements, we focused on two areas within PMRF implicated in driving these movements: gigantocellular nucleus (Gi) and paramedian pontine reticular formation (PPRF)[19,55–61].

We asked whether Gi and PPRF are specialized for head and eye movements, as studies in cats and primates have yielded mixed effects, and this question has not been addressed in mice[62]. To achieve selective stimulation, we pursued an anterograde viral approach to express ChR2 in Gi or PPRF neurons that receive input from SC (Figure 5A, B)[63,64]. No labeled cell bodies were observed in SC, indicating that tectoreticular neurons were not retrogradely infected (Figure 5A, B). We measured attempted head movements and saccades evoked by optogenetically stimulating SC-recipient Gi and PPRF neurons. Activation of SC-recipient Gi neurons elicited attempted head movements but very few saccades, whereas activation of SC-recipient PPRF neurons elicited conjugate saccades but very few attempted head movements, indicating that Gi and PPRF represent separate, specialized modules for the head and eyes, respectively (Figure C, D).

Next, we characterized the displacements and endpoints of movements elicited by optogenetic stimulation of SC-recipient Gi and PPRF modules. Both Gi-evoked attempted head movements and PPRF-evoked saccades were exclusively leftward (ipsiversive), consistent with the stereotypical lateralization of brainstem motor pathways (Figure 5E, F, K, L). This was also consistent with the uniform directionality of SC-evoked head movements in freely moving and head-fixed mice, but marked a transition from the mixture of saccade directions elicited by SC stimulation (Figure 2B–C, Figure 3B–G). Strikingly, similar to SC-evoked head and eye movements, Gi-evoked attempted head displacements were nearly invariant to initial eye position, whereas PPRF-evoked saccade displacements were strongly dependent on initial eye position (variance explained by initial eye position: 0.02 ± 0.04 [head] vs. 0.34 ± 0.22 [saccade]; mean ± S.D.; $p = 0.002$, $n = 9$ per region, Welch's t-test) (Figure 5E, F, K, L, M–P). Taken together, these results suggest that SC innervates independent modules in Gi and PPRF that transform identical excitatory input into head movements with stereotyped displacements and saccades with stereotyped endpoints, respectively.

Individual tectoreticular neurons collateralizing to Gi and PPRF drive both head and eye movements

Although SC innervates both Gi and PPRF and drives both head and eye movements, previous experiments could not determine whether single tectoreticular axons collateralize to both structures or whether separate tectoreticular subpopulations innervate each. To distinguish between these possibilities, we asked whether neurons projecting to one structure innervate the other, using a retrograde labeling approach. To avoid labeling fibers of passage, we injected the more distal structure, Gi, with retrogradely infecting virus encoding Cre, and we injected SC with a virus encoding a Cre-dependent tdTomato (Figure 6A, C, E). For comparison, in a separate cohort we injected SC with an AAV encoding a constitutively expressed tdTomato to provide pan-neuronal labeling (Figure 6B, D, F). In both cohorts, we observed tdTomato-labeled axon terminals in similar spatial distributions in PPRF and Gi, including in the areas targeted for optogenetic stimulation of SC-recipient neurons, indicating that individual tectoreticular axons collateralize to both Gi and PPRF (Figure 6C–F, Figure 5A, B).

We next asked whether tectoreticular neurons that collateralize in PPRF and Gi can drive both head and eye movements, or whether separate tectoreticular populations are needed (Figure 6G). To distinguish between these possibilities, we optogenetically stimulated SC terminals in Gi while blocking antidromically evoked recurrent activity within SC, which could recruit non-Gi-projecting SC neurons, by injecting TTX into SC (Figure 6H, I). In the control condition, stimulating SC terminals in Gi elicited antidromic spiking in SC (Figure 6J, P, Q) and both attempted head and eye movements similar to those elicited by SC stimulation (Figure 6K, L, R–T, Figure 1, Figure 2). After TTX injection, stimulating SC axon terminals did not elicit antidromic spikes in SC (Figure 6M, P, Q) but continued to evoke attempted head movements and saccades indistinguishable from those evoked in the control condition (Figure 6N, O, R–T). These data thus indicate that tectoreticular axons with collaterals in Gi and PPRF are able to evoke both head and eye movements in the absence of recurrent dynamics or recruitment of additional cells in SC. Taken together, these anatomical and functional data suggest that individual tectoreticular neurons are able to drive both head movements with stereotyped displacements and saccades with stereotyped endpoints by collateralizing to distinct, computationally specialized target populations in Gi and PPRF.

Gi and PPRF modules execute different computations—The preceding recording, tracing, and stimulation experiments suggested that Gi and PPRF execute distinct transformations of tectoreticular activity to determine head displacements and to compute saccade endpoints and displacements. To test this hypothesis, we performed extracellular recordings in each structure (Figure 7A, B). Similar to tectoreticular neurons, Gi and PPRF neurons displayed biphasic responses to whisker stimulation (Figure 7D, Fig 4C, Figure S6, Figure S7). However, whereas tectoreticular and Gi populations showed similar tuning preferences for airpuff location (Figure 7E), PPRF neurons as a population were less biased in their preference for left whisker airpuffs (tectoreticular: 0.66; 35/53; Gi: 0.50; 90/179; PPRF: 0.41; 120/292; p =0.001 [PPRF vs. tectoreticular]; p = 0.06 [PPRF vs. Gi]; Fisher's exact test) (Figure 7E). This was consistent with the behavioral observation that airpuffs

drive attempted head movements almost exclusively toward the side of the stimulated whiskers (96 ± 5% toward, mean ± S.D., n = 9 mice) but bidirectional saccades (54 ± 12% toward, mean ± S.D., n = 9 mice).

To compare movement-related activity in Gi and PPRF, we regressed attempted head displacement, saccade displacement, and saccade endpoint against firing rate for each neuron (Figure 7G, I, K). As with stimulus side, the population tuning preferences of Gi neurons resembled those of tectoreticular neurons (Figure 7G, I, K). In contrast, tuning in PPRF differed significantly from tectoreticular and Gi tuning for head displacement and saccade displacement, and differed significantly from Gi tuning for saccade endpoint (Figure 7G, I, K). Consistent with the observation that stimulating PPRF drives ipsiversive saccades, the difference in saccade displacement tuning was due to an increase in the proportion of PPRF neurons tuned for leftward saccades (PPRF: 0.19; 55/292; tectoreticular: 0.02; 1/53; Gi: 0.08; 15/179; p = 0.001 [PPRF vs. tectoreticular]; p = 0.002 [PPRF vs. Gi]; Fisher's exact test). Tuned neurons were enriched in a dorsal portion of the recorded area in PPRF (Figure S5).

To determine whether saccade tuning was an emergent property of SC-recipient PPRF neurons, we performed additional recordings in optotagged SC-recipient PPRF neurons (Figure 7C, Figure S6, Figure S7). We observed different tuning in SC-recipient PPRF neurons compared to tectoreticular neurons for stimulus location, head displacement, saccade displacement, and saccade endpoint (Figure 7D–K). The difference in saccade tuning was due to an increase in the proportion of neurons tuned for saccade endpoints left of center (tectoreticular: 0.06; 3/53; tagged PPRF: 0.23; 8/35; p = 0.023 [tectoreticular vs. tagged PPRF]; Fisher's exact test) and leftward saccade displacements (tectoreticular: 0.02; 1/53; tagged PPRF: 0.20; 7/35; p = 0.006 [tectoreticular vs. tagged PPRF]; Fisher's exact test), consistent with a model wherein PPRF neurons transform SC input to compute saccade parameters. Taken together, these data suggest that Gi and PPRF are independent, dedicated subcircuits that differentially process SC activity to drive head movements with stereotyped displacements and saccades with stereotyped endpoints, respectively.

Discussion

Here we investigated the neural mechanisms that underlie coordinated movements. To address this question, we pursued a systematic approach to interrogate the neural coordination of mouse gaze. By stimulating and recording at different levels in the mouse gaze hierarchy, we unexpectedly revealed that no individual stage in this anatomical hierarchy computes the desired overall displacement. Instead, single upper motor neurons specify a mixture of head displacements and eye endpoints, with displacements for different body parts computed independently and at distinct anatomical stages. As such, the computations within this anatomical hierarchy do not follow a straightforward progression from higher-order parameters down to the level of individual body parts. The multiplexing of displacements and endpoints for different body parts by single upper motor neurons in SC is enabled by dedicated hindbrain modules for each body part. These Gi and PPRF modules differentially process SC input, transforming identical excitatory drive into head movements with stereotyped displacements and saccades with stereotyped endpoints, respectively. These

findings thus broaden the space of conceptual models of movement coordination, revealing a non-hierarchical computational logic implemented within an anatomical hierarchy.

In primates and cats, SC neurons encode the overall gaze displacement but not necessarily the individual eye and head displacements[35,37,38,65,66]. Although analogous stimulation studies found that mouse SC harbors topographic head and eye motor maps, it was not determined what movement parameters (e.g., overall gaze displacement or individual head and eye displacements) were encoded. There were, however, hints that mice differed from cats and primates[31,48]. For example, one study reported the puzzling observation that sustained (> 250 ms) tectoreticular activation in freely moving mice evoked a series of stepwise head movements, reminiscent of the saccade "staircase" evoked by sustained SC microstimulation in head-fixed primates. In contrast, sustained tectoreticular stimulation in head-fixed mice evoked only a single saccade, not a staircase[31,39]. By accounting for initial head and eye position, we determined that the topographic motor maps in mouse SC correspond to head displacements and saccade endpoints. This result may explain why sustained mouse tectoreticular stimulation did not elicit saccade staircases: A single saccade brought the eyes to the endpoint specified by the stimulated SC ensemble[31]. Most importantly, because the saccade displacement needed to reach a given endpoint varies with initial eye position, our results revealed that mouse SC, unlike cat and primate SC, does not specify overall gaze displacements (Figure 1).

A potential benefit of stereotyping saccade endpoints is ensuring the eyes return to the center by anticipating head movements and their associated image-stabilizing VOR eye movements[67]. Such a coding strategy may underlie the widespread yet unexplained observation in most vertebrate species (i.e., those lacking a high-acuity retinal specialization such as a fovea, including birds, frogs, mice, and rabbits) that the eyes tend to return to the orbital centers after gaze shifts, a phenomenon known as recentering[42,45,67,68]. In this model, saccades themselves do not recenter the eyes, but instead anticipate and offset the subsequent head movementevoked slow VOR eye movement, thereby ensuring the eyes settle in a central final position. This may explain why saccade endpoint eccentricity scales with anteroposterior location in SC, paralleling head displacement amplitude: larger head movements elicit larger slow VOR movements that must be offset by more eccentric saccade endpoints. Together, these results provide a candidate mechanism to explain how mice can use head movements to shift gaze and saccades to ensure the eyes recenter.

Gaze shifts belong to a large and varied group of complex, reflexive behaviors that involve coordinated movements of multiple body parts and end in a stereotyped pose, e.g., the hand or forepaw at the mouth during consummatory behaviors. Other examples include escape, approach, predation, grooming, courtship, and aggressive behaviors[9–11,17,18,23,69–71]. Interestingly, many of these behaviors can also be triggered by activating specific subcortical regions and cell types[9,10,18,69–71]. In the future, it will be important to determine whether these movements are coordinated using a strategy similar to that of mouse SC tectoreticular neurons, i.e., simultaneously specifying a mixture of displacements and endpoints for different body parts.

Individual SC neurons are able to simultaneously specify head displacements and saccade endpoints because they engage dedicated, computationally specialized brainstem modules for different body parts. Beyond ensuring coordinated movements end in a stereotyped pose, this generalizable modular architecture may offer additional benefits to the organism. First, a modular architecture may facilitate the evolution of the neural control of movements tailored to the anatomy and ethology of different species. For example, whereas mouse SC drives head movements with stereotyped displacements and saccades with stereotyped endpoints, the mechanics of gaze shifts differ in owls, which do not move their eyes, and mammalian species with high-acuity retinal specializations (e.g., foveae) such as cats and primates, where SC encodes overall gaze displacement[35,37,38,72–74]. A similar diversification is observed for other body parts, e.g., the forelimb takes the form of an arm in a human, a flipper in a whale, and a wing in a bat, with each articulated differently[75]. Second, modules encoding movement endpoints for certain body parts may facilitate feedback control and course correction[15,76].

Limitations of the study

We found that individual tectoreticular neurons collateralize to both PPRF and Gi to drive both head and eye movements. These collaterals may be the reason saccades without head movements are rarely observed in rodents (and other afoveates), whereas primates frequently generate saccades independently of head movements to foveate salient stimuli[67]. Nevertheless, subpopulations of mouse SC neurons may innervate only PPRF or Gi, as has been observed in primates[77,78]. Such populations would be difficult to detect using the approaches in this study. Instead, sparse labeling and reconstruction of the axonal arbors of SC neurons would be needed, as has been undertaken for other brain areas by the Janelia MouseLight project[79].

We found that the representations of stimulus location and head and eye movement parameters within SC, Gi, and PPRF differ. Although our findings suggest that the computations performed within Gi and PPRF differ, they do not reveal how these computations are implemented. First, because many of these variables are correlated, e.g., stimulus location and head movement direction, analytical tools such as generalized linear models may facilitate more granular investigation of these computations. Second, it will be critical to define the circuit logic in PPRF and Gi. Although our analyses suggest that SC-recipient Gi neurons are a relay for head displacement signals from SC, putative relays elsewhere in the brain, e.g., primary sensory thalamus, were subsequently shown to perform sophisticated computations, including attentional gating and surround modulation[80]. What afferents may provide gating or other modulatory cues to Gi will be important to investigate in the future. In contrast to Gi, it is evident in our data that neurons within or downstream of PPRF transform SC activity into the desired saccade endpoint and the displacement needed to reach that endpoint from the initial position of the eyes. PPRF is believed to comprise at least two cell types, long-latency burst neurons (LLBNs) and excitatory burst neurons (EBNs), that form a putative network topology of SC→LLBN→EBN→abducens motor neurons[81]. In the future, it will be important to identify the cell types within this circuit that compute saccade endpoint and displacement and the source of the eye position information that enables the transformation from endpoint to displacement.

In addition to further unraveling how SC, Gi, and PPRF control the horizontal component of gaze shifts, future work should determine whether the logic we have identified applies to SC control of mouse gaze movements in other axes, which are thought to be controlled by distinct downstream circuitry[19]. There are additional key differences between gaze movements in these axes, e.g., whereas the eye movements that accompany head yaw are conjugate, changes in head pitch are accompanied by non-conjugate vergence eye movements[43–45]. These vergence eye movements are believed to be driven by otolith-mediated sensing of head pitch, but the underlying circuitry is not understood[82,83]. In the future, an approach similar to that in the present study may enable deconstruction of the circuitry controlling gaze in other axes.

The gaze shifts we have studied are a reflexive, unlearned form of coordinated movement, but many coordinated movements are skills honed through repetition and are generated volitionally. These behaviors, such as playing the piano, are thought to involve distinct neural hierarchies that include forebrain areas such as cortex and basal ganglia. It is unclear whether the computational logic identified in this study will generalize to those circuits[20,22,84–86]. Nevertheless, the approach we have applied to systematically deconstruct transformations at downstream structures may be useful for investigating these pathways. Moreover, although differences between systems are likely, our model may provide a useful point of comparison in efforts to unravel computations within other motor hierarchies.

STAR Methods

Resource availability

Lead contact—Further information or requests for reagents and resources should be addressed to the lead contact, Evan Feinberg (evan.feinberg@ucsf.edu).

Materials availability—This study did not generate new unique reagents.

Data and code availability

- Primary data are available at Zenodo. The DOI is listed in the key resources table.
- Custom analysis code is available in a GitHub repository. The address is listed in the key resources table.
- Any additional information required to reanalyze the data reported in this paper is available from the lead contact upon request.

Experimental model and study participant details

Animals—All experiments were performed in accordance with protocols approved by the UCSF Institutional Animal Care and Use Committee. Male C57BL/6J wild- type (Jackson Laboratory, stock 000664) mice between 2 and 6 months of age were used. Mice were group housed in a vivarium with a reversed 12:12 h light:dark cycle and tested during the dark phase. No statistical methods were used to predetermine sample size.

Behavioral experiments were not performed blinded as the experimental setup and analyses are automated.

Methods details

Surgical procedures—Mice were administered meloxicam (5 mg/kg) 30 min prior to surgery. Anesthesia was induced with inhalation of 2.5% isoflurane and buprenorphine (1.5 mg/kg) was administered at the onset of the procedure. Isoflurane (0.5–2.5% in oxygen, 1 L/min) was used to maintain anesthesia and adjusted based on the mouse's breath and reflexes. Ocular gel was used to protect the eyes from dehydration. Once anesthetized, Nair was used to remove hair from the scalp and the surgical area was disinfected using alchohol and iodine wipes. Following surgery, mice were allowed to recover in their home cages for at least 1 week.

The skull was exposed by removing a 5 mm diameter circle of skin using spring scissors. Prior to viral injections, a small hole was drilled in the skull using a 0.5 mm burr dental drill. Viruses were delivered to the target brain regions using pulled glass pipettes coupled to a microsyringe pump (UMP3T-1, World Precision Instruments) controlled by a stereotaxic frame (Model 940, Kopf Instruments). A titanium headplate was cemented to the leveled skull (Metabond, Parkell). For optogenetic manipulations, fiber optic cannulae were constructed from ceramic ferrules (CFLC440–10, Thorlabs) and optical fiber (400 μm core, 0.39 NA, FT400UMT) using lowautofluorescence epoxy (F112, Eccobond). Cannulae were targeted using a cannula holder (Thorlabs, XCL) coupled to a stereotaxic frame.

To prepare animals for freely moving recordings, the female end of a Mill-Max connector (Mill-Max Manufacturing Corp. 853-93-100-10-001000) was cut to 5 mm (2 rows of 4 columns) and cemented to the rostral end of the mouse's headplate. Camera assemblies were reversibly attached via this connector during recording sessions.

For electrical microstimulation and electrode recordings, a 1 mm craniotomy was performed with a 0.5 mm burr dental drill over right SC (centered around ML: 1.1 mm, AP: 0.6 mm relative to lambda), left PPRF (centered around ML: 0.5 mm, AP: −0.5 mm relative to lambda), or left Gi (centered around ML: 0.4 mm, AP: −1.4 mm relative to lambda). A ~2 mm-high Metabond well was constructed around the craniotomy to retain saline during recording sessions. Craniotomies were performed 18–24 hours in advance of recordings and filled with removable silicone sealant (Kwik-Cast). In addition, a screw was inserted into the skull rostral to bregma and attached to a ground wire.

Freely moving behavior—Timing and synchronization of the freely moving behavior were controlled by a microcontroller (Arduino MEGA, 2560 Rev3, Arduino) receiving serial commands from MATLAB. All behavioral and data acquisition timing information was recorded by a NI DAQ (USB-6001) for post hoc alignment. Mice were allowed to move freely on a custom transparent platform measuring 8" x 8". Body tracking was accomplished using a camera (Flir, BFS-U3-28S5M-C) recording at 100 Hz from below the animal. The mouse was illuminated from two sides with visible light, and a black backdrop was placed above the platform to provide contrast. The platform was mounted on a turntable (18635A54, McMaster-Carr) that was periodically rotated to avoid tangling of the wires. To

measure eye movements, two miniature cameras (1937, Adafruit) were used. Each camera was fitted with a miniature bandpass filter (Filter Opt Cast IR 5 mm, Edmund Optics) and both were mounted on the head using a 3D-printed camera holder. One IR LED was used to illuminate each eye and generate a corneal reflection for computing angular eye position. Videos of both the left and right eyes were recorded at 90 Hz. To measure head movements, a 9-axis inertial measurement unit (IMU)(HMT-00203, Rosco Technologies) recording at 100 Hz was mounted to the camera holder.

Head-fixed behavior—During experiments, mice were secured in a 3D-printed mouse holder. Timing and synchronization of the behavior were controlled by a microcontroller (Arduino MEGA 2560 Rev3, Arduino) receiving serial commands from MATLAB. All behavioral and data acquisition timing information was recorded by a NI DAQ (USB-6001) for post hoc alignment. The movements of the left and right eyes were monitored at 100 Hz using two cameras (BFS-U328S5M-C, Flir) coupled to 110 mm working distance 0.5 X telecentric lenses (#67-303, Edmund Optics). A bandpass filter (FB850-40, Thorlabs) was attached to the lens to block visible illumination. Three IR LEDs (475-1200-ND, DigiKey) were used to illuminate the eye and one was aligned to the camera's vertical axis to generate a corneal reflection. Attempted head rotations were measured using a 3D-printed headplate holder coupled to a load cell force sensor (Sparkfun, SEN-14727). Load cell measurements (sampling frequency 80 Hz) were converted to analog signals and recorded using a NI DAQ (sampling frequency 2000 Hz).

Electrical microstimulation—Electrical stimulation experiments were performed in head-fixed mice using a 16-channel Neuronexus probe (A4×4–4mm-200-200-1250-A16) arranged as a linear array of four shanks spaced by 200 μm. Each shank housed four linearly arranged electrodes separated by 200 μm. Electrodes had large surface areas (1250 μm^2) capable of delivering large currents. Prior to insertion, probe shanks were coated with DiI (1 mM, Thermo Fisher Scientific) to permit histological reconstruction of the probe track. The probe's ground wire was attached to a cortical skull screw and the craniotomy was filled with saline. The probe was oriented along the anterior-posterior axis and lowered into SC through intact dura using a micromanipulator (Sensapex, uMp-4) at a speed of 5 μm/s to the desired depth. We focused on the anterior-posterior axis in SC because head-fixed mice make predominantly horizontal eye movements and earlier studies suggested that horizontal saccade displacements are represented along this SC axis[42–45,92]. Probes were allowed to settle for 15 minutes before a stimulation session. Microstimulation was achieved using an Intan RHS stimulation-recording system and Intan software. Stimuli consisted of biphasic pulses (0.2 ms per phase) delivered for 10 ms with amplitudes of 30–60 μA. The electrode array was lowered to 1.5 mm below dura and then incrementally advanced while the distal electrodes were tested. Depths and stimulation currents were selected as the shallowest and lowest values, respectively, that regularly evoked saccades using each shank. Experiments consisted of 400–480 pseudorandomly interleaved stimulation trials (100–120 per shank) separated by inter-trial intervals drawn from a 5–10 s uniform distribution. SC electrical microstimulation data were obtained from nine mice and mice underwent one session each.

Whisker airpuff behavior—Airpuffs were applied to the whiskers of head-fixed mice to evoke directionally biased attempted head and eye movements. Airpuff stimuli were generated using 3D-printed airpuff nozzles (1.5 mm wide, 10 mm long), spaced 24 mm apart, and centered 10 mm beneath the mouse's left and right whiskers. Airpuff nozzles were connected to compressed air (5 psi) that was gated by a solenoid. For tectoreticular loss-of-function experiments, left and right stimuli were randomly selected and presented at intervals drawn from a 7–12 s uniform distribution. Each session consisted of 350 stimulus presentations and lasted ~55 minutes. For SC, PPRF, and Gi electrophysiological recordings, left and right stimuli were randomly selected and presented at intervals drawn from a 3–7 s uniform distribution. Each session consisted of 700 stimulus presentations and lasted ~60 minutes. For electrophysiological recordings, only mice with a high probability of generating touch-evoked saccades (>50 saccades/session) were used. Other than this screening process, no training or habituation was performed.

Optogenetic stimulation and inhibition—Fiber optic cables were coupled to implanted fibers and the junction was shielded with black heat shrink. A 470 nm fiber-coupled LED (M470F3, Thorlabs) was used to excite ChR2-expressing neurons, and a 554 nm fiber-coupled LED (MINTF4, Thorlabs) was used to inhibit eNpHR3.0-expressing neurons.

For optogenetic activation of SC neurons in freely-moving mice, a 1:1 mixture of *AAV1.hSyn.ChR2(H134R)-eYFP* and *AAV1-CAG.tdTomato* was injected in right SC (0.6 AP, 1.1 ML, −2.1 and −1.9 DV; 100 nl per depth), and a fiber was implanted over the injection site (0.6 AP, 1.1 ML, −2.0 DV). Experiments were performed 14–24 days post-injection. LED intensity was individually set to evoke an orienting movement without a flinching response (0.5–1.5 mW). Each session consisted of 700 stimulation trials (100 ms duration, 2–5 s interval) and lasted ~40 minutes. Mice underwent three sessions each.

For optogenetic activation of SC-recipient Gi or PPRF neurons in head-fixed mice, *AAV1.hSyn.Cre* was injected into right SC (0.6 AP, 1.1 ML, −1.9 and −2.1 DV; 100 nl per depth), a 1:1 mixture of *AAV1.EF1a.DIO.hChR2(H134R)-eYFP* and *AAV1.CAG-FLEX-tdTomato* was injected into left PPRF (−0.5 AP, 0.5 ML, −4.7 and −4.9 DV; 100 nl per depth) or left Gi (−1.4 AP, 0.4 ML, −5.25, −5.5, −5.75, and −6.0 DV; 100 nl per depth), and an optic fiber was implanted over left PPRF (−0.5 AP, 0.5 ML, −4.7 DV) or left Gi (−1.4 AP, 0.4 ML, −5.3 DV). Experiments were performed 14–31 days post-injection. Each session consisted of 350 stimulation trials (40 ms duration, 8.5 mW intensity, 7–12 s interval) and lasted ~55 minutes. Mice underwent one session each.

For optogenetic activation of abducens motor neurons, *Chat-Cre* mice (Jackson Laboratory strain 108957) were injected with a 1:1 mixture of *AAV1.EF1a.DIO.hChR2(H134R)-eYFP* and *AAV1.CAG-FLEX-tdTomato* in left abducens (−1.1 AP, 0.4 ML, −4.6, and −4.8 DV; 50 nl per depth), and an optic fiber was implanted over abducens (−1.1 AP, 0.4 ML, −4.55 DV). Experiments were performed 14 days post-injection. LED intensity was individually set to evoke a ~5° eye movement (0.037–1.75 mW). Each session consisted of 350 stimulation trials (500 ms, 7–12 s interval). Mice underwent one session each.

For optogenetic inhibition of tectoreticular neurons during the whisker airpuff behavior, mice were injected with *HSV-hEF1α-cre* in left PMRF(−0.8 AP, 0.4 ML, −4.7, −4.9, −5.1 DV; 100 nl per depth) and a 1:1 mixture of *AAV1.EF1a.DIO.eNpHR3.0-eYFP* and *AAV1.CAG-FLEX-tdTomato* in right SC (0.6 AP, 1.1 ML, −2.1 and −1.9 DV; 100 nl per depth), and an optic fiber was implanted over right SC (0.6 AP, 1.1 ML, −2.0 DV). Experiments were performed 21–50 days post-injection. Each session consisted of 350 whisker airpuff trials, and light (8.5 mW) was delivered to SC for 1 s centered around airpuff onset on a random 50% of trials. Mice underwent 6 whisker airpuff sessions each.

Pharmacological silencing of SC—For optogenetic activation of SC axon terminals in head-fixed mice, a 1:1 mixture of *AAV1.hSyn.ChR2(H134R)-eYFP* and *AAV1-CAG.tdTomato* was injected in right SC (0.6 AP, 1.1 ML, −2.1 and −1.9 DV; 100 nl per depth), and an optic fiber was implanted over left Gi (−1.4 AP, 0.4 ML, −5.3 DV). Experiments were performed 10–20 days post-injection. Each mouse underwent an initial control session before undergoing an experimental session (+TTX) session the following day. Each session consisted of 350 stimulation trials and identical light intensities were used for each mouse across days (40 ms duration, 1–2 mW intensity, 7–12 s interval). One hour before the experimental session, 100 nL of either saline or tetrodotoxin-citrate (Alomone Labs, T-550; 40 μm) was injected in right SC (0.6 AP, 1.1 ML, −2.0 DV). All mice displayed prominent ipsiversive circling behavior following TTX injection, consistent with SC silencing. During both the control and TTX sessions, an electrode was inserted in SC (see Single-unit recordings) to detect the presence or absence of neural activity. In two of the animals, additional electrode recordings were performed to confirm TTX-mediated silencing at least 2 mm ventral and 1 mm anterior of the injection site, suggesting that all of SC was silenced.

Single-unit recordings—Acute recordings were performed in head-fixed mice using either a 128-channel Neuronexus probe (A4×32-Poly2-5mm-23s-200-177) or a 64-channel Cambridge NeuroTech optrode (ASSY-77 H6, 100 μm core lambda-b fiber with 300 μm horizontal separation between the probe and fiber). Prior to insertion, probe shanks were coated with DiI (1 mM, Thermo Fisher Scientific) to allow post hoc histological reconstruction of the probe track, the probe's ground wire was attached to the skull screw, and the craniotomy was covered in saline. The probe was lowered using a micromanipulator (Sensapex) through intact dura at a speed of 5 μm/s to 100 μm below the desired depth, and then raised at a speed of 2 μm/s to the desired depth. The probe was allowed to settle for at least 25 minutes before recording began. Mice underwent multiple recording sessions on successive days unless their craniotomies showed signs of decay (e.g., dura no longer intact, signs of bleeding, or scar tissue formation). Craniotomies were covered with silicone (Kwik-Cast) between sessions. Extracellular potentials were acquired using an Intan RHS recording system and Intan RHX software.

Optotagging—Tectoreticular neurons were identified using antidromic optotagging. A 1:1 mixture of *AAV1.hSyn.ChR2(H134R)-eYFP* and *AAV1-CAG.tdtomato* was injected in right SC (0.6 AP, 1.1 ML, −2.1 and −1.9 DV; 100 nl per depth), and a 400 μm fiber was implanted in left contralateral medial PMRF (−0.8 AP, −0.4 ML, −4.7 DV). After ten days, animals

were screened for ChR2 expression by determining whether head and eye movements were evoked by light pulses (470 nm, 40 ms, 1 mW) delivered to PMRF. Recordings were performed 10–30 days post-injection. Tectoreticular neurons were identified as those antidromically activated by photostimulating axon terminals in the contralateral medial PMRF. At the beginning and end of each recording session, 20 pulses of 470 nm light (5 ms pulse duration, separated by 100 ms, 1 mW intensity) were delivered through an optical fiber implanted over PMRF. Neurons were classified as tectoreticular (10–38% of neurons recorded in a given session) if they reliably responded to photostimulation (>80% response rate) with short latency (<5 ms), low temporal jitter (<2 ms), and with similar waveforms as spontaneous action potentials (correlation coefficient > 0.90).

We used an optrode to identify SC-recipient PPRF neurons. First, *AAV1.hSyn.Cre* was injected into right SC (0.6 AP, 1.1 ML, −2.0 DV; 150 nl), and a 1:1 mixture of *AAV1.EF1a.DIO.hChR2(H134R)-eYFP* and *AAV1.CAG-FLEX-tdTomato* was injected into left PPRF (−0.5 AP, 0.5 ML, −4.7 and −4.9 DV; 100 nl per depth). Optagging experiments were performed 10–20 days post-injection. SC-recipient PPRF neurons were identified as those activated by photostimulating PPRF somata using a 473 nm fiber-coupled laser (Shanghai Laser & Optics Century). At the beginning and end of each recording session, 20 pulses of 470 nm light (10 ms pulse duration, separated by 100 ms, 10 mW intensity) were delivered through a 100 μm diameter optical fiber attached to the probe. Neurons were classified as SC-recipient (4–44% of neurons recorded in a given session) if they reliably responded to photostimulation (>80% response rate) with short latency (<10 ms), low temporal jitter (<2 ms), and with similar waveforms as spontaneous action potentials (correlation coefficient > 0.90).

Tracing—To examine axon collaterals of Gi-projecting SC neurons, mice were injected with *HSV-hEF1aCre* in left Gi (−1.4 AP, 0.4 ML, −5.5 and −5.75 DV; 100 nl per depth), and *AAV1.CAG-FLEXtdTomato* in right SC (0.6 AP, 1.1 ML, −2.0 DV; 150 nl). To examine the axon collaterals of pan-neuronal SC neurons, a separate cohort of mice were injected with a 1:1 mixture of *AAV1hSyn.HI.eGFP-Cre and AAV1.CAG-FLEX-tdTomato* in right SC (0.6 AP, 1.1 ML, −2.0 DV; 100 nl). Mice were euthanized 14 days post-injection and their brains were histologically processed and imaged.

Histology—For histological confirmation of electrode placements, fiber placements, injection sites, and for tracing experiments, mice were perfused with PBS followed by 4% paraformaldehyde (PFA). Brains were removed and fixed overnight in 4% PFA and stored in 20% sucrose solution for at least 1 day. Brains were sectioned at 50 μm thickness using a cryostat (NX70, Cryostar), mounted, and coverslipped using DAPI mounting medium (Southern Biotech). For histological confirmation of electrode placements, fiber placements, and injection sites, tile scans were acquired using a confocal microscope (LSM700, Zeiss) coupled to a 10X air objective. For quantifying SC tectoreticular axonal projections, Z-stack tile scans (10 μm spacing) were acquired using a confocal microscope coupled to a 10X air objective.

Quantification and statistical analysis

Anatomical reconstructions and analysis—Confocal tile scans of coronal brain sections were manually registered to the Allen Mouse Common Coordinate Framework, Version 3 (Allen CCF) and anatomical points of interest (e.g., the tips of electrode and fiber tracks) were manually identified using a MATLAB-based GUI (Shamash et al., 2018). Briefly, each brain section image was matched to a 2D slice through the Allen CCF reference volume, common landmarks were identified between the brain section and reference image, and the section image was warped to align with the reference image using affine transformations. For visualization, reconstructed anatomical features were projected onto 2D coronal slices through the Allen CCF reference volume. AP and DV coordinates are reported relative to the origin of the Allen CCF volume (the anterior, superior, right corner) and ML coordinates were reported relative to the midline (5700 μm from the right edge of the volume).

To quantify SC projections, coronal brain section images were registered to Allen CCF and a rolling-ball background subtraction was performed to level variance in background autofluorescence. Images were binarized at a threshold determined to isolate axonal and terminal processes. Expression was quantified by binning pixels into 50 μm blocks (heatmaps) or averaging a 300 μm thick horizontal stripe (line profiles). Data from sections were normalized to peak (heatmaps) or area under curve (line profiles) before averaging to show proportional expression within each structure.

Allen CCF unit coordinates from single unit recordings were reconstructed by identifying the electrical channel with the largest amplitude spike waveform and using the probe's geometry and insertion angle of incidence to estimate coordinates relative to the tip. Probe insertion relative to the Allen CCF was determined to be angled slightly posterior (−7°). Random jitter (±10 μm) was added to unit coordinates to prevent eclipsing in scatter plots. Unit tunings were identified using methods described below ("Electrophysiological Analysis"). Two-dimensional density plots were generated using Gaussian kernel-density estimates and plotting six equally spaced density lines from 30–100% of the of highest density.

Freely moving behavior analysis—Body camera videos were processed post hoc using DeepLabCut[89]. The network was trained to detect six features on the mouse: nose, chest, abdomen, tail base, and the two camera LEDs. Frames were excluded if the platform was moving or if any of the tracked points had a DeepLabCut-calculated likelihood of $p < 0.99$. Eye camera videos were processed post hoc using DeepLabCut. The network was trained to detect the top, bottom, left and right edges of the pupil and the left and right edges of the corneal reflection. Frames with a DeepLabCut-calculated likelihood of $p < 0.99$ were excluded from analysis. The pupil data were interpolated to match the body camera sampling rate (100 Hz), and angular eye position was determined using a previously described method developed for C57BL/6J[93].

Head yaw position was determined by integrating the IMU yaw velocity. To obtain the angle of the head relative to the body (used to determine starting head-body posture), the instantaneous yaw angle of the head relative to the body was calculated using the nose,

chest, and abdomen features extracted using DeepLabCut. For each timepoint, the direction of the head was found as the vector **h** between the chest and nose, and the direction of the body was the vector **b** between the abdomen and chest. The angle between these vectors was found using the dot product: $\theta = \cos^{-1}[(\mathbf{h} \cdot \mathbf{b}) / (|\mathbf{h}| |\mathbf{b}|)]$, and the sign was determined using the cross product. To organize head movement traces by starting head-body angle, the IMU-derived head positions for each trial were aligned according to the video-derived head-body angle. Head movement detection was adapted from[31]. We focused on yaw head rotations because SC stimulation-evoked movements were primarily along the yaw axis (Figure S1B). Head movements were identified when angular velocity exceeded 140°/s in the same direction for at least 30 ms. Head movement onset and offset were found by moving backward or forward, respectively, in time from the seed location until velocity fell below 28°/s or velocity direction changed. Total head movement amplitude was the difference between the head positions at offset and onset (Figure S1B).

We observed two distinct phases of eye motion: a fast saccadic phase coinciding with head movement onset followed by a slow phase whose magnitude was roughly equal and opposite to the ongoing head rotation (Figure 1C). This slow phase resembled a gaze-stabilizing reflex driven by vestibular feedback (vestibulo ocular reflex, VOR)[42,45,92]. We focused our analyses on the horizontal component of the fast saccadic phase because evoked saccades were primarily confined to the horizontal axis (Figure S1A). Saccades were identified separately for left and right pupils. Seed positions for tentative saccades were identified as timepoints where pupil velocity exceeded 550°/s in the horizontal axis. To ensure that saccades were not counted more than once, a seed time point was only considered if it was the local maximum velocity within a ±50 ms time window. To identify the saccade onset and offset, a ±50 ms window around each seed was oversampled by a factor of two (5 ms resolution). Saccade onset and offset were defined as the first time point where velocity fell below 70°/s or changed direction. If neither of those criteria were met, onset or offset was set at ±35 ms. Saccade amplitude was the difference between the pupil positions at offset and onset. For putative saccades to be included in analysis, both pupils needed to make saccade-like movements in the same direction within 30 ms of each other. Saccades displayed a main sequence, i.e., peak velocity scaled linearly with amplitude, and saccade amplitude was highly correlated between eyes (Figure S1C–E). Stimulus-evoked movements were defined as saccades or head movements occurring in the 100 ms period following optogenetic stimulation onset. To distinguish stimulation-evoked saccades from spontaneously occurring saccades, we only considered trials in which the eyes and head were stationary in the 50 ms and 100 ms, respectively, preceding stimulation onset. Furthermore, to exclude VOR-induced saccades, we only examined saccades in which the eyes remained stationary between stimulation onset and saccade onset. The head and eye components of stimulation-evoked gaze shifts were defined as the amplitude of the saccadic phase of eye motion and the distance traveled by the head between head movement onset and saccade offset, respectively. Eye or head position dependence was quantified using linear regression (Figure 1).

Head-fixed behavior analysis—Eye camera videos were processed post hoc using DeepLabCut. The network was trained to detect the left and right edges of the pupil and

the left and right edges of the corneal reflection. Frames with a DeepLabCut-calculated likelihood of $p < 0.99$ were discarded from analysis. Eye position was defined as the average of the left and right pupil positions minus the mean. Saccades were defined as eye movements that exceeded 100°/s, were at least 3° in amplitude, and were not preceded by a saccade in the previous 100 ms. The initial positions and endpoints of saccades were defined as the first points at which saccade velocity rose above 30°/s and fell below 20°/s, respectively. Analyses focused on horizontal saccades because saccades in head-fixed mice are strongly confined to the azimuth. Raw attempted head rotation data were low-pass filtered at 80 Hz using a zero-phase second-order Butterworth filter, interpolated to match the pupil sampling rate (100Hz), and Z-scored. For some experiments, behavioral sessions for individual mice were combined across days.

Stimulus-evoked saccades were defined as saccades occurring in the 100 ms period following stimulus onset (i.e., microstimulation, optogenetic excitation, or airpuff delivery), and stimulus-evoked head movements were defined as the head-sensor reading 80 ms post-stimulus onset. A stimulus was deemed to have evoked a head movement if the magnitude of the head movement exceeded 0.2 Z. To examine the eye position-dependence of stimulus-evoked saccades, only trials in which the eyes were stationary in the 500 ms period preceding stimulus onset were used. To examine the eye position-dependence of stimulus-evoked head movements, only trials in which the head was stationary in the 500 ms period preceding stimulus onset were used. Eye position-dependence was quantified using linear regression with Z-scored standardized variables.

Classifying electrical stimulation site was performed on data from individual mice using multinomial logistic regression. Predictors (saccade amplitude and saccade endpoint) were Z-score standardized. Data were randomly subsampled to include an equal number of values per class (shank). Cross validation was used to train multinomial logistic regression models and test fold predictions were used to compute accuracy. This process was repeated 100 times and the mean accuracy was used as the measure of predictor performance. Randomly shuffling shank labels for saccade amplitude or saccade endpoint before cross validation resulted in accuracies of ~0.25, consistent with chance.

Electrophysiological analysis—Spike sorting was performed using KiloSort2.5 software[87,88] followed by manual curation using Phy2 (https://github.com/cortex-lab/phy). Units with an average firing rate below 0.2 Hz, more than 1% of detected events with an absolute refractory period <1 ms, significant amplitude drift across the recording session, or atypical waveforms were excluded.

All units were pooled for analysis. Firing rate traces were smoothed with a 10 ms Gaussian window for display purposes. For each unit, tuning for puff side was determined by comparing spike counts in the 50 ms following puff onset in left versus right puff trials (two-tailed t-test, $p < 0.05$). To identify motor-tuned units, spike counts in the 50 ms following puff onset were regressed against head displacement, saccade displacement, or saccade endpoint. Tuned units were defined as those with a linear regression P-value below 0.05, and preference for left versus right movements was determined using the sign of the regression slope. For head movement tuning analyses, only trials in which mice did not move their head

in the 100 ms prior to stimulus onset were used. For saccade tuning analyses, only trials in which mice did not saccade in the 100 ms prior to stimulus onset were used. A Chi-squared test was used to compare the proportions of left-preferring, right-preferring, and untuned units across brain regions. A binomial test was used to determine tuning preference within each brain region.

Targeted dimensionality reduction was used to examine the population dynamics of SC activity during touch-evoked gaze shifts. We pooled all n units from different sessions and mice for analysis. Our goal was to identify $n \times 1$ vectors that maximally accounted for response variance due to each behavioral variable. We then sought to visualize population dynamics in this subspace. We refer to these vectors as the coding dimension (**CD**), and computed **CD** for left vs. right stimulus locations, head displacements, saccade displacements, and saccade endpoints. **CD** was computed by subtracting the average spike count during the 50 ms window following airpuff onset for left - right trials, and dividing this $n \times 1$ vector by its length. We then projected population activity aligned to stimulus onset in left trials ($x(t)_{left}$) and right trials ($x(t)_{right}$) along **CD** ($CD^T x$). This allowed us to visualize population dynamics in a behaviorally relevant subspace. Selectivity was defined as the difference between left and right projections ($CD^T x_{left} - CD^T x_{right}$). To visualize projections and determine significance, we used bootstrapping across units. Each bootstrap consisted of resampling units with replacement and computing **CD**s de novo. Traces show bootstrapped median values and shading indicates 1–99% confidence intervals.

Supplementary Material

Refer to Web version on PubMed Central for supplementary material.

Acknowledgments:

We thank A. Basbaum, M. Brainard, K. Ganguly, Z. Knight, A. Krishnaswamy, D. Manoli, A. Nelson, M. Scanziani, and all members of the Feinberg laboratory for helpful discussions and/or comments on the manuscript. The top-down mouse schema was adapted from https://doi.org/10.5281/zenodo.3925903 and the side profile mouse was adapted from https://doi.org/10.5281/zenodo.3925901. This work was supported by the National Institutes of Health (grants DP2MH119426 and NS109060 to E.H.F.) and the Sandler Foundation.

References

1. Kandel ER, Schwartz JH, Jessell TM, Siegelbaum SA & Hudspeth AJ. (2013) Principles of Neural Science, Fifth Editon | Neurology Collection | McGraw-Hill Medical. 2013.
2. Miall RC & Wolpert DM. (1996) Forward models for physiological motor control. Neural Networks 9, 1265–1279. 10.1016/s0893-6080(96)00035-4. [PubMed: 12662535]
3. Wolpert DM, Miall RC & Kawato M. (1998) Internal models in the cerebellum. Trends Cogn. Sci. 2, 338–347. 10.1016/s1364-6613(98)01221-2. [PubMed: 21227230]
4. Kawato M. (1999) Internal models for motor control and trajectory planning. Curr. Opin. Neurobiol. 9, 718–727. 10.1016/s0959-4388(99)00028-8. [PubMed: 10607637]
5. Graziano MSA, Taylor CSR & Moore T. (2002) Complex movements evoked by microstimulation of precentral cortex. Neuron 34, 841–851. 10.1016/s0896-6273(02)00698-0. [PubMed: 12062029]
6. Overduin SA, d'Avella A, Carmena JM & Bizzi E. (2012) Microstimulation Activates a Handful of Muscle Synergies. Neuron 76, 1071–1077. 10.1016/j.neuron.2012.10.018. [PubMed: 23259944]

7. Bizzi E, Giszter SF, Loeb E, Mussa-Ivaldi FA & Saltiel P. (1995) Modular organization of motor behavior in the frog's spinal cord. Trends Neurosci. 18, 442–446. 10.1016/0166-2236(95)94494-p. [PubMed: 8545910]
8. D'Avella A, Saltiel P & Bizzi E. (2003) Combinations of muscle synergies in the construction of a natural motor behavior. Nat. Neurosci. 6, 300–308. 10.1038/nn1010. [PubMed: 12563264]
9. Ruder L et al. (2021) A functional map for diverse forelimb actions within brainstem circuitry. Nature 590, 445–450. 10.1038/s41586-020-03080-z. [PubMed: 33408409]
10. Ferreira-Pinto MJ et al. (2021) Functional diversity for body actions in the mesencephalic locomotor region. Cell 184, 4564–4578.e18. 10.1016/j.cell.2021.07.002. [PubMed: 34302739]
11. Ruder L & Arber S. (2019) Brainstem Circuits Controlling Action Diversification. Annu. Rev. Neurosci. 42, 485–504. 10.1146/annurev-neuro-070918-050201. [PubMed: 31283898]
12. Graziano MSA & Aflalo TN. (2007) Mapping Behavioral Repertoire onto the Cortex. Neuron 56, 239–251. 10.1016/j.neuron.2007.09.013. [PubMed: 17964243]
13. Wang X et al. (2017) Deconstruction of Corticospinal Circuits for Goal-Directed Motor Skills. Cell 171, 440–455.e14. 10.1016/j.cell.2017.08.014. [PubMed: 28942925]
14. Todorov E & Jordan MI. (2002) Optimal feedback control as a theory of motor coordination. Nat. Neurosci. 5, 1226–1235. 10.1038/nn963. [PubMed: 12404008]
15. Merel J, Botvinick M & Wayne G. (2019) Hierarchical motor control in mammals and machines. Nat. Commun. 10, 1–12. 10.1038/s41467-019-13239-6. [PubMed: 30602773]
16. Diedrichsen J, Shadmehr R & Ivry RB. (2010) The coordination of movement: optimal feedback control and beyond. Trends Cogn. Sci. 14, 31–39. 10.1016/j.tics.2009.11.004. [PubMed: 20005767]
17. Shang C et al. (2019) A subcortical excitatory circuit for sensory-triggered predatory hunting in mice. Nat. Neurosci. 22, 909–920. 10.1038/s41593-019-0405-4. [PubMed: 31127260]
18. Xie Z et al. (2022) A brain-to-spinal sensorimotor loop for repetitive self-grooming. Neuron 110, 874–890.e7. 10.1016/j.neuron.2021.11.028. [PubMed: 34932943]
19. Isa T, Marquez-Legorreta E, Grillner S & Scott EK. (2021) The tectum/superior colliculus as the vertebrate solution for spatial sensory integration and action. Curr. Biol. 31, R741–R762. 10.1016/j.cub.2021.04.001. [PubMed: 34102128]
20. Shenoy KV, Sahani M & Churchland MM. (2013) Cortical Control of Arm Movements: A Dynamical Systems Perspective. Annu. Rev. Neurosci. 36, 337–359. 10.1146/annurev-neuro-062111-150509. [PubMed: 23725001]
21. Park J, Coddington LT & Dudman JT. (2020) Basal Ganglia Circuits for Action Specification. Annu. Rev. Neurosci. 43, 485–507. 10.1146/annurev-neuro-070918-050452. [PubMed: 32303147]
22. Guo JZ et al. (2015) Cortex commands the performance of skilled movement. Elife 4, 10.7554/elife.10774.
23. Arber S & Costa RM. (2022) Networking brainstem and basal ganglia circuits for movement. Nat. Rev. Neurosci. 23, 342–360. 10.1038/s41583-022-00581-w. [PubMed: 35422525]
24. Nelson A, Abdelmesih B & Costa RM. (2021) Corticospinal populations broadcast complex motor signals to coordinated spinal and striatal circuits. Nat. Neurosci. 2021 2412 24, 1721–1732. 10.1038/s41593-021-00939-w.
25. Ugolini G & Kuypers HGJM. (1986) Collaterals of corticospinal and pyramidal fibres to the pontine grey demonstrated by a new application of the fluorescent fibre labelling technique. Brain Res. 365, 211–227. 10.1016/0006-8993(86)91632-x. [PubMed: 2418921]
26. Kita T & Kita H. (2012) The subthalamic nucleus is one of multiple innervation sites for long-range corticofugal axons: a single-axon tracing study in the rat. J. Neurosci. 32, 5990–5999. 10.1523/jneurosci.5717-11.2012. [PubMed: 22539859]
27. Keizer K & Kuypers HGJM. (1989) Distribution of corticospinal neurons with collaterals to the lower brain stem reticular formation in monkey (Macaca fascicularis). Exp. Brain Res. 1989 742 74, 311–318. 10.1007/bf00248864.
28. Lemon RN. (2008) Descending pathways in motor control. Annu. Rev. Neurosci. 31, 195–218. 10.1146/annurev.neuro.31.060407.125547. [PubMed: 18558853]

29. Hooks BM et al. (2018) Topographic precision in sensory and motor corticostriatal projections varies across cell type and cortical area. Nat. Commun. 9, 10.1038/s41467-018-05780-7.
30. Komiyama T et al. (2010) Learning-related fine-scale specificity imaged in motor cortex circuits of behaving mice. Nature 464, 1182–1186. 10.1038/nature08897. [PubMed: 20376005]
31. Masullo L et al. (2019) Genetically Defined Functional Modules for Spatial Orienting in the Mouse Superior Colliculus. Curr. Biol. 29, 10.1016/j.cub.2019.07.083.
32. Takahashi M, Sugiuchi Y, Izawa Y & Shinoda Y. (2005) Commissural excitation and inhibition by the superior colliculus in tectoreticular neurons projecting to omnipause neuron and inhibitory burst neuron regions. J. Neurophysiol. 94, 1707–1726. 10.1152/jn.00347.2005/asset/images/large/z9k0090548660013.jpeg. [PubMed: 16105954]
33. Isa K et al. (2020) Dissecting the Tectal Output Channels for Orienting and Defense Responses. eNeuro 7, 1–18. 10.1523/eneuro.0271-20.2020.
34. Grantyn A, Moschovakis AK & Kitama T. (2004) Control of orienting movements: role of multiple tectal projections to the lower brainstem. Prog. Brain Res. 143, 423–438. 10.1016/s0079-6123(03)43040-9. [PubMed: 14653185]
35. Freedman EG. (2008) Coordination of the Eyes and Head during Visual Orienting. Exp. Brain Res. 190, 369. 10.1007/s00221-008-1504-8. [PubMed: 18704387]
36. Guitton D. (1992) Control of eye-head coordination during orienting gaze shifts. Trends Neurosci. 15, 174–179. 10.1016/0166-2236(92)90169-9. [PubMed: 1377424]
37. Bergeron A, Matsuo S & Guitton D. (2003) Superior colliculus encodes distance to target, not saccade amplitude, in multi-step gaze shifts. Nat. Neurosci. 2003 64 6, 404–413. 10.1038/nn1027.
38. Sajad A, Sadeh M & Crawford JD. (2020) Spatiotemporal transformations for gaze control. Physiol. Rep. 8, 1–22. 10.14814/phy2.14533.
39. Schiller PH & Stryker M. (1972) Single-unit recording and stimulation in superior colliculus of the alert rhesus monkey. J. Neurophysiol. 35, 915–924. 10.1152/jn.1972.35.6.915. [PubMed: 4631839]
40. Bizzi E, Kalil RE & Morasso P. (1972) Two modes of active eye-head coordination in monkeys. Brain Res. 40, 45–48. 10.1016/0006-8993(72)90104-7. [PubMed: 4624490]
41. Zahler SH, Taylor DE, Wong JY, Adams JM & Feinberg EH. (2021) Superior colliculus drives stimulus-evoked directionally biased saccades and attempted head movements in head-fixed mice. Elife 10, 10.7554/elife.73081.
42. Meyer AF, O'Keefe J & Poort J. (2020) Two Distinct Types of Eye-Head Coupling in Freely Moving Mice. Curr. Biol. 30, 2116–2130.e6. 10.1016/j.cub.2020.04.042. [PubMed: 32413309]
43. Meyer AF, Poort J, O'Keefe J, Sahani M & Linden JF. (2018) A Head-Mounted Camera System Integrates Detailed Behavioral Monitoring with Multichannel Electrophysiology in Freely Moving Mice. Neuron 100, 46–60.e7. 10.1016/j.neuron.2018.09.020. [PubMed: 30308171]
44. Wallace DJ et al. (2013) Rats maintain an overhead binocular field at the expense of constant fusion. Nature 498, 65–69. 10.1038/nature12153. [PubMed: 23708965]
45. Michaiel AM, Abe ET & Niell CM. (2020) Dynamics of gaze control during prey capture in freely moving mice. Elife 9, 10.7554/elife.57458.
46. Rossi J et al. (2011) Melanocortin-4 receptors expressed by cholinergic neurons regulate energy balance and glucose homeostasis. Cell Metab. 13, 195–204. 10.1016/j.cmet.2011.01.010. [PubMed: 21284986]
47. Stahl JS et al. (2015) Mechanics of mouse ocular motor plant quantified by optogenetic techniques. J. Neurophysiol. 114, 1455–1467. 10.1152/jn.00328.2015. [PubMed: 26108953]
48. Wang L, Liu M, Segraves MA & Cang J. (2015) Visual experience is required for the development of eye movement maps in the mouse superior colliculus. J. Neurosci. 35, 12281–12286. 10.1523/jneurosci.0117-15.2015. [PubMed: 26338338]
49. Moschovakis AK, Karabelas AB & Highstein SM. (1988) Structure-function relationships in the primate superior colliculus. II. Morphological identity of presaccadic neurons. J. Neurophysiol. 60, 263–302. 10.1152/jn.1988.60.1.263. [PubMed: 3404220]
50. Yizhar O, Fenno LE, Davidson TJ, Mogri M & Deisseroth K. (2011) Optogenetics in Neural Systems. Neuron 71, 9–34. 10.1016/j.neuron.2011.06.004. [PubMed: 21745635]

51. Redgrave P, Mitchell IJ & Dean P. (1987) Descending projections from the superior colliculus in rat: a study using orthograde transport of wheatgerm-agglutinin conjugated horseradish peroxidase. Exp. Brain Res. 68, 147–167. 10.1007/bf00255241. [PubMed: 2826204]
52. Lima SQ, Hromádka T, Znamenskiy P & Zador AM. (2009) PINP: A New Method of Tagging Neuronal Populations for Identification during In Vivo Electrophysiological Recording. PLoS One 4, 6099. 10.1371/journal.pone.0006099.
53. Li N, Daie K, Svoboda K & Druckmann S. (2016) Robust neuronal dynamics in premotor cortex during motor planning. Nature 532, 459–464. 10.1038/nature17643. [PubMed: 27074502]
54. Castro-Alamancos M & Favero M. (2016) Whisker-related afferents in superior colliculus. J Neurophysiol 115, 2265–2279. 10.1152/jn.00028.2016. [PubMed: 26864754]
55. Bouvier J et al. (2015) Descending Command Neurons in the Brainstem that Halt Locomotion. Cell 163, 1191–1203. 10.1016/j.cell.2015.10.074. [PubMed: 26590422]
56. Cregg JM et al. (2020) Brainstem neurons that command mammalian locomotor asymmetries. Nat. Neurosci. 2020 236 23, 730–740. 10.1038/s41593-020-0633-7.
57. Schwenkgrub J, Harrell ER, Bathellier B & Bouvier J. (2020) Deep imaging in the brainstem reveals functional heterogeneity in V2a neurons controlling locomotion. Sci. Adv. 6, 10.1126/sciadv.abc6309.
58. Usseglio G, Gatier E, Heuzé A, Hérent C & Bouvier J. (2020) Control of Orienting Movements and Locomotion by Projection-Defined Subsets of Brainstem V2a Neurons. Curr. Biol. 30, 4665–4681.e6. 10.1016/j.cub.2020.09.014. [PubMed: 33007251]
59. Sparks DL, Barton EJ, Gandhi NJ & Nelson J. (2002) Studies of the role of the paramedian pontine reticular formation in the control of head-restrained and head-unrestrained gaze shifts. Ann. N. Y. Acad. Sci. 956, 85–98. 10.1111/j.1749-6632.2002.tb02811.x. [PubMed: 11960796]
60. Gioia M & Bianchi R. (1992) Intrinsic Organization of the Paramedian Pontine Reticular Formation of the Cat. Cells Tissues Organs 144, 127–134. 10.1159/000147296.
61. Chimoto S, Iwamoto Y, Shimazu H & Yoshida K. (1996) Monosynaptic activation of medium-lead burst neurons from the superior colliculus in the alert cat. J. Neurophysiol. 75, 2658–2661. 10.1152/jn.1996.75.6.2658. [PubMed: 8793771]
62. Gandhi NJ, Barton EJ & Sparks DL. (2008) Coordination of eye and head components of movements evoked by stimulation of the paramedian pontine reticular formation. Exp. Brain Res. 189, 35–47. 10.1007/s00221-008-1401-1. [PubMed: 18458891]
63. Zingg B et al. (2017) AAV-Mediated Anterograde Transsynaptic Tagging: Mapping Corticocollicular Input-Defined Neural Pathways for Defense Behaviors. Neuron 93, 33–47. 10.1016/j.neuron.2016.11.045. [PubMed: 27989459]
64. Zingg B, Peng B, Huang J, Tao HW & Zhang LI. (2020) Synaptic Specificity and Application of Anterograde Transsynaptic AAV for Probing Neural Circuitry. J. Neurosci. 40, 3250–3267. 10.1523/jneurosci.2158-19.2020. [PubMed: 32198185]
65. Freedman EG, Stanford TR & Sparks DL. (1996) Combined eye-head gaze shifts produced by electrical stimulation of the superior colliculus in rhesus monkeys. J. Neurophysiol. 76, 927–952. 10.1152/jn.1996.76.2.927. [PubMed: 8871209]
66. Paré M, Crommelinck M & Guitton D. (1994) Gaze shifts evoked by stimulation of the superior colliculus in the head-free cat conform to the motor map but also depend on stimulus strength and fixation activity. Exp. Brain Res. 101, 123–139. 10.1007/bf00243222. [PubMed: 7843291]
67. Land MF. (2019) The Evolution of Gaze Shifting Eye Movements. in Curr. Top. Behav. Neurosci. 41, 3–11. 10.1007/7854_2018_60. [PubMed: 30120752]
68. Land MF & Nilsson D-E. (2012) Animal Eyes. Oxford Anim. Biol. Ser. (Oxford Univerity Press).
69. Hoy JL, Bishop HI & Niell CM. (2019) Defined Cell Types in Superior Colliculus Make Distinct Contributions to Prey Capture Behavior in the Mouse. Curr. Biol. 29, 4130–4138.e5. 10.1016/j.cub.2019.10.017. [PubMed: 31761701]
70. Lin D et al. (2011) Functional identification of an aggression locus in the mouse hypothalamus. Nature 470, 221–227. 10.1038/nature09736. [PubMed: 21307935]
71. Evans DA et al. (2018) A synaptic threshold mechanism for computing escape decisions. Nature 558, 590–594. 10.1038/s41586-018-0244-6. [PubMed: 29925954]

72. Freedman E & Sparks D. (1997) Eye-head coordination during head-unrestrained gaze shifts in rhesus monkeys. J. Neurophysiol. 77, 2328–2348. 10.1152/jn.1997.77.5.2328. [PubMed: 9163361]
73. Freedman E, Stanford T & Sparks D. (1996) Combined eye-head gaze shifts produced by electrical stimulation of the superior colliculus in rhesus monkeys. J. Neurophysiol. 76, 927–952. 10.1152/jn.1996.76.2.927. [PubMed: 8871209]
74. Knudsen EI. (1989) Fused binocular vision is required for development of proper eye alignment in barn owls. Vis. Neurosci. 2, 35–40. 10.1017/s0952523800004302. [PubMed: 2487636]
75. Krubitzer LA & Prescott TJ. (2018) The Combinatorial Creature: Cortical Phenotypes within and across Lifetimes. Trends Neurosci. 41, 744–762. 10.1016/j.tins.2018.08.002. [PubMed: 30274608]
76. Todorov E. (2004) Optimality principles in sensorimotor control. Nat. Neurosci. 7, 907–915. 10.1038/nn1309. [PubMed: 15332089]
77. Scudder CA, Kaneko CR & Fuchs AF. (2002) The brainstem burst generator for saccadic eye movements: A modern synthesis. Exp. Brain Res. 142, 439–462. 10.1007/s00221-001-0912-9. [PubMed: 11845241]
78. Moschovakis AK, Karabelas AB & Highstein SM. (1988) Structure-function relationships in the primate superior colliculus. I. Morphological classification of efferent neurons. J. Neurophysiol. 60, 232–262. 10.1152/jn.1988.60.1.232. [PubMed: 3404219]
79. Winnubst J et al. (2019) Reconstruction of 1,000 Projection Neurons Reveals New Cell Types and Organization of Long-Range Connectivity in the Mouse Brain. Cell 179, 268–281.e13. 10.1016/j.cell.2019.07.042. [PubMed: 31495573]
80. Sherman SM. (2007) The thalamus is more than just a relay. Curr. Opin. Neurobiol. 17, 417–422. 10.1016/j.conb.2007.07.003. [PubMed: 17707635]
81. Keller EL, McPeek RM & Salz T. (2000) Evidence against direct connections to PPRF EBNs from SC in the monkey. 84, 1303–1313. 10.1152/jn.2000.84.3.1303.
82. Oommen BS & Stahl JS. (2008) Eye orientation during static tilts and its relationship to spontaneous head pitch in the laboratory mouse. Brain Res. 1193, 57–66. 10.1016/j.brainres.2007.11.053. [PubMed: 18178173]
83. Khan SI, Della Santina CC & Migliaccio AA. (2019) Angular vestibuloocular reflex responses in otop1 mice. I. otolith sensor input is essential for gravity context-specific adaptation. J. Neurophysiol. 121, 2291–2299. 10.1152/jn.00811.2018. [PubMed: 30969887]
84. Dudman JT & Krakauer JW. (2016) The basal ganglia: From motor commands to the control of vigor. Curr. Opin. Neurobiol. 37, 158–166. 10.1016/j.conb.2016.02.005. [PubMed: 27012960]
85. Peters AJ, Liu H & Komiyama T. (2017) Learning in the Rodent Motor Cortex. Annu. Rev. Neurosci. 40, 77–97. 10.1146/annurev-neuro-072116-031407. [PubMed: 28375768]
86. Strick PL, Dum RP & Rathelot JA. (2021) The Cortical Motor Areas and the Emergence of Motor Skills: A Neuroanatomical Perspective. Annu. Rev. Neurosci. 44, 425–447. 10.1146/annurev-neuro-070918-050216. [PubMed: 33863253]
87. Pachitariu M, Sridhar S & Stringer C. (2023) Solving the spike sorting problem with Kilosort. bioRxiv 10.1101/2023.01.07.523036.
88. Steinmetz NA et al. (2021) Neuropixels 2.0: A miniaturized high-density probe for stable, long-term brain recordings. Science 372, 10.1126/science.abf4588.
89. Mathis A et al. (2018) DeepLabCut: markerless pose estimation of user-defined body parts with deep learning. Nat. Neurosci. 21, 1281–1289. 10.1038/s41593-018-0209-y. [PubMed: 30127430]
90. Shamash P, Carandini M, Harris K & Steinmetz N. (2018) A tool for analyzing electrode tracks from slice histology. bioRxiv 10.1101/447995.
91. Claudi F et al. (2021) Visualizing anatomically registered data with brainrender. Elife 10, 10.7554/elife.65751.
92. Payne HL & Raymond JL. (2017) Magnetic eye tracking in mice. Elife 6, 10.7554/elife.29222.
93. Sakatani T & Isa T. (2007) Quantitative analysis of spontaneous saccade-like rapid eye movements in C57BL/6 mice. Neurosci. Res. 58, 324–331. 10.1016/j.neures.2007.04.003. [PubMed: 17482700]

Highlights

- Superior colliculus (SC) specifies head displacement and saccade endpoint in mice
- Single SC neurons collateralize in pons and medulla to coordinate the eyes and head
- A subpopulation in pons transforms SC activity into saccade endpoints
- A subpopulation in medulla transforms SC activity into head displacements

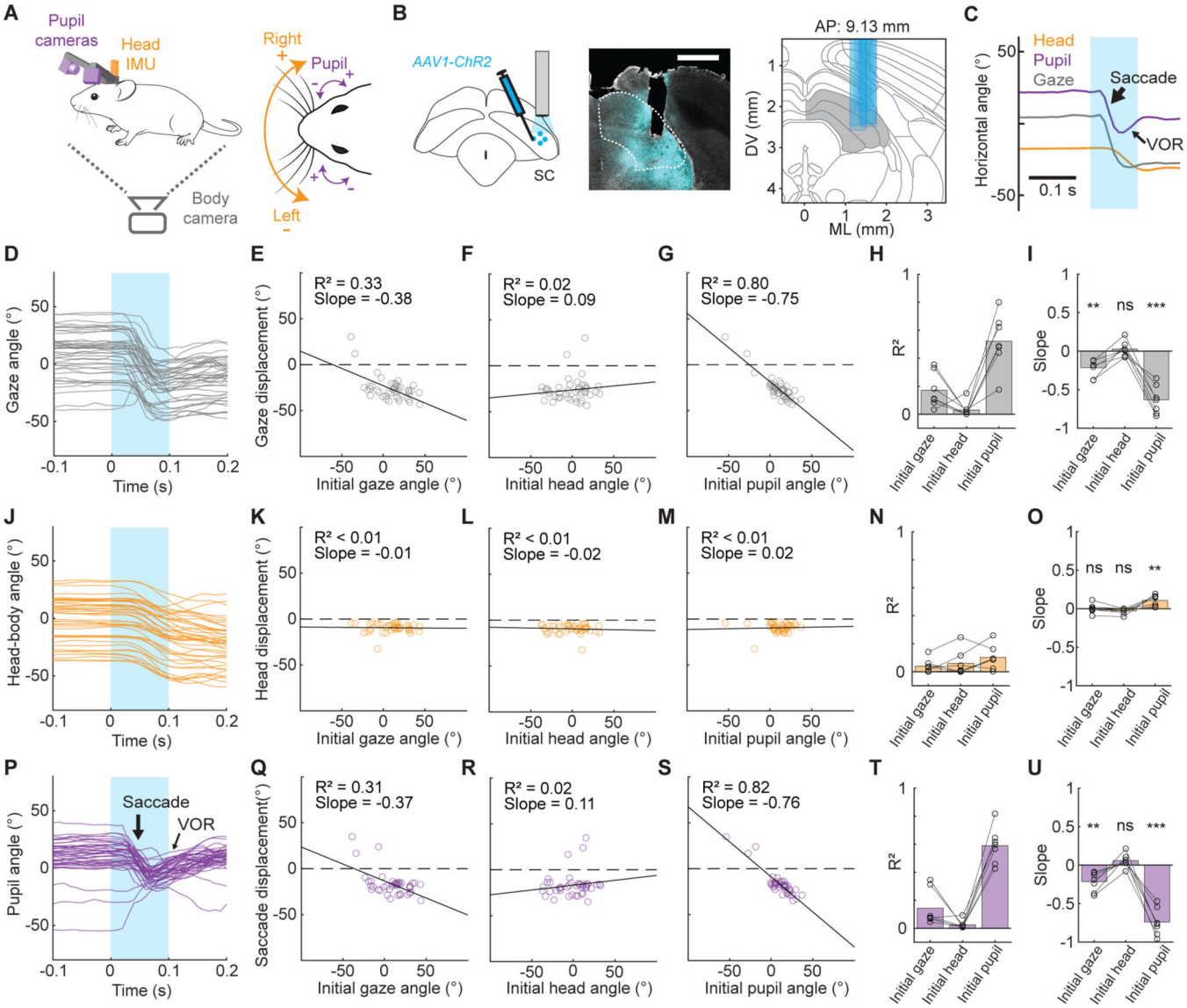

Figure 1. Superior colliculus specifies head displacement and saccade endpoint but not overall gaze displacement in freely moving mice.

A, Left, schematic. Head-mounted cameras and inertial measurement unit track eyes and head, respectively. Initial head-eye angle is tracked using camera below transparent platform. Right, sign conventions adopted throughout this paper. **B**, Optogenetic strategy. Left, schematic. Center, sample histology. Scale bar, 1 mm. Right, fiber placements for all mice (n = 7) in Allen common coordinate framework (CCF). **C**, Example head, pupil, and gaze traces illustrating stimulation-evoked gaze shift. Blue bar indicates LED stimulation period. Note two distinct phases of eye motion: a fast saccadic phase coinciding with head movement onset followed by a slow phase with roughly equal and opposite to the head rotation, resembling a gaze-stabilizing reflex (vestibular ocular reflex, VOR). **D-G, J-M, P-S**, Data for example mouse. **D**, Gaze traces aligned to LED onset. **E-G**, Relationship between gaze displacement and initial gaze angle (E), initial head angle (F), and initial pupil angle (G). **H, I** Population summary of R^2 and slopes for ChR2-evoked gaze displacement

regressed against initial gaze, head, or pupil angles. **J**, Head movement traces aligned to LED onset. **K-M**, Relationship between head displacement and initial gaze angle (K), initial head angle (L), and initial pupil angle (M) **N, O**, Population summary of R^2 (N) and slope (O) for optogenetically evoked head displacement regressed against initial gaze, head, or pupil angles. **P**, Pupil traces aligned to LED onset. **Q-S**, Relationship between pupil displacement and initial gaze angle (Q), initial head angle (R), and initial pupil angle (S). **T, U**, Population summary of R^2 (T) and slope (U) for optogenetically evoked pupil displacement regressed against initial gaze, head, or pupil angles. See also Figure S1.

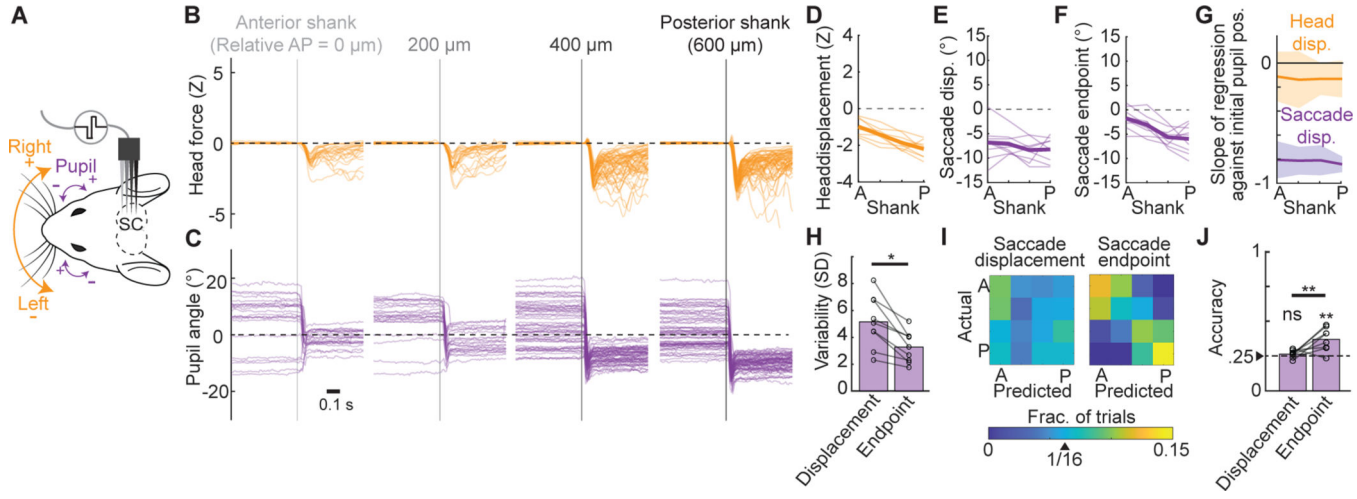

Figure 2. Mouse superior colliculus comprises topographic maps of head displacement and saccade endpoint.

A, Schematic of electrical microstimulation. **B, C**, Attempted head movement (B) and pupil angle (C) traces aligned to stimulation onset (gray shading) for each electrode for an example animal. **D-F**, Population summary of attempted head displacements (D), saccade displacements (E), and saccade endpoints (F) as a function of microstimulation site. Thin lines are data from individual animals (n = 9). Thick line is population mean. **G**, Fraction of saccade displacement or attempted head displacement variance (R^2, linear regression) explained by initial pupil position across animals (mean ± SD). **H**, Variability of saccade displacements and endpoints. Each point is the mean shank-wise variance. Lines denote individual mice, bars denote population means. **I**, Confusion matrices of predicted versus actual microstimulation shank for example animal. The matrix cell values indicate the fraction of trials with that result. Chance level indicated with triangle. A, anterior. P, posterior. **J**, Summary of classifier accuracies predicting microstimulation shank using saccade displacement or endpoint. Chance level indicated with triangle and dashed line. Confusion matrix and accuracy scores are from test folds of cross-validated multinomial logistic regressions. Lines connect values for individual mice, bars are population means. Orange denotes head data and purple denotes eye data. Statistics performed using one- or two-sample Student's t-test (*p < 0.05; **p < 0.01; ***p < 0.001; ns, not significant). See also Figure S2.

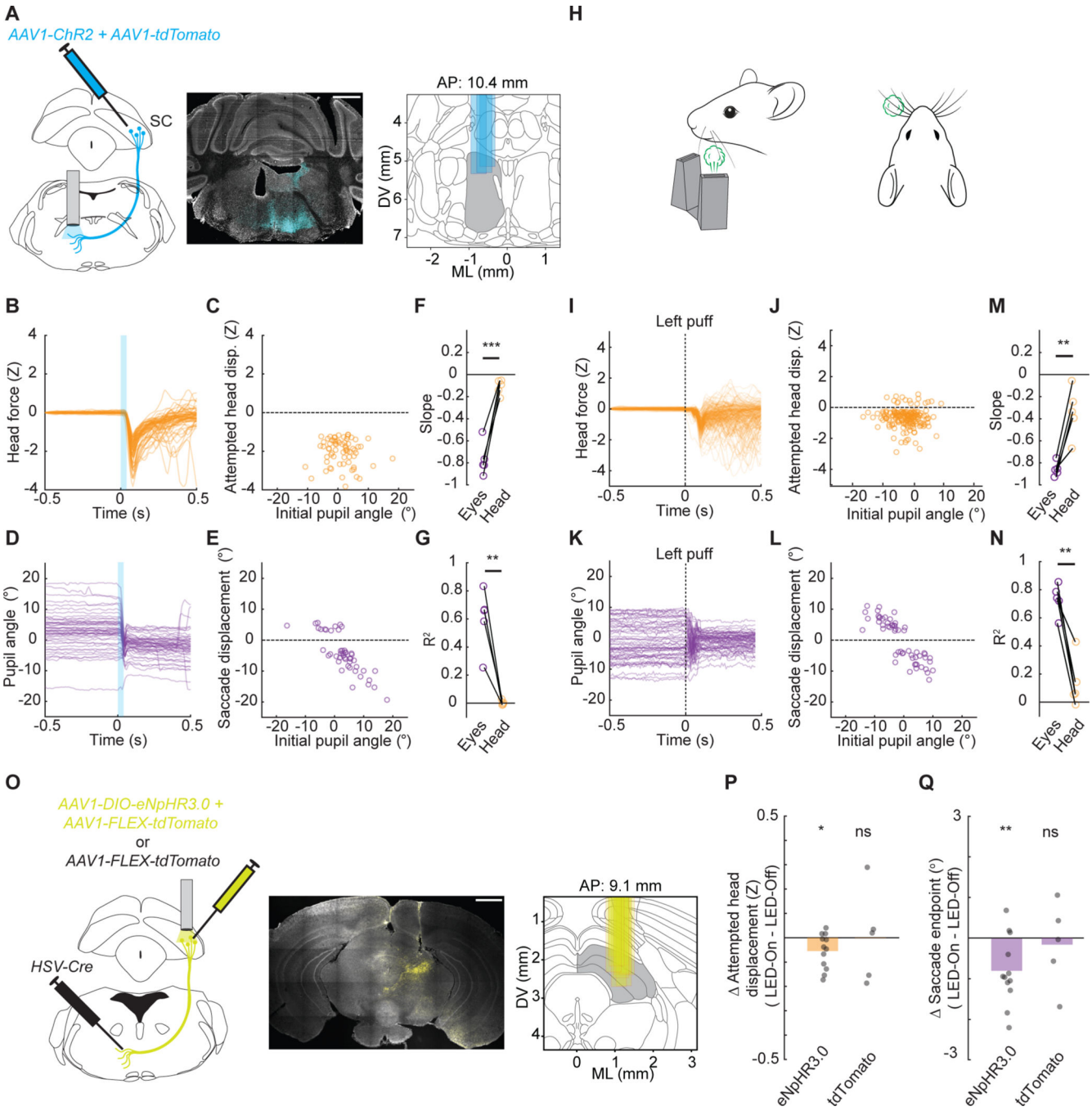

Figure 3. Tectoreticular neurons drive sensory-guided eye and head movements with stereotyped endpoints and displacements, respectively.

A, Left, schematic. Middle, sample histology. Scale bar, 1 mm. Right, fiber placements in Allen CCF (n = 5 mice). **B**, Attempted head movement traces aligned to LED onset (blue shading) for an example animal. **C**, Relationship between initial pupil angle and attempted head displacement for traces in **B**. **D**, Pupil angle traces aligned to LED onset (blue shading). **E**, Relationship between initial pupil angle and saccade displacement for traces in **D**. Data in **B-D** were derived from the same animal. **F, G** Population summary

of slopes and R^2 of head displacements and saccade displacements regressed against initial pupil angle. Markers denote individual animals. **H**, Schematics illustrating airpuff stimulation of the left whisker bundle. **I**, Attempted head movement traces aligned to left whisker airpuff onset (vertical dashed line) for an example animal. **J**, Relationship between initial pupil angle and attempted head displacement for traces in **I**. **K**, Pupil position traces aligned to whisker airpuff onset (vertical dashed line). **L**, Relationship between initial pupil angle and saccade displacement for traces in **K**. Data in **I-L** were derived from the same animal. **M, N**, Population summary of slopes (M) and R^2 (N) for regression of airpuff-evoked head displacements and saccade displacements against initial pupil angle. Markers denote individual animals. **O**, Left, schematic illustrating strategy to optogenetically inhibit tectoreticular neurons (n = 12 mice). Tectoreticular activity was suppressed in the period surrounding whisker airpuff onset. A separate cohort was prepared to control for effects of optogenetic excitation (n = 5 mice). Middle, sample histology. Scale bar, 1 mm. Right, fiber placements in Allen CCF. **P**, Change in mean attempted head displacement between LED-On and LED-Off whisker airpuff trials. **Q**, As in **P** for saccade endpoint. Orange denotes head data and purple denotes eye data. Statistics performed using Student's t-test (*$p < 0.05$; **$p < 0.01$; ***$p < 0.001$; ns, not significant).

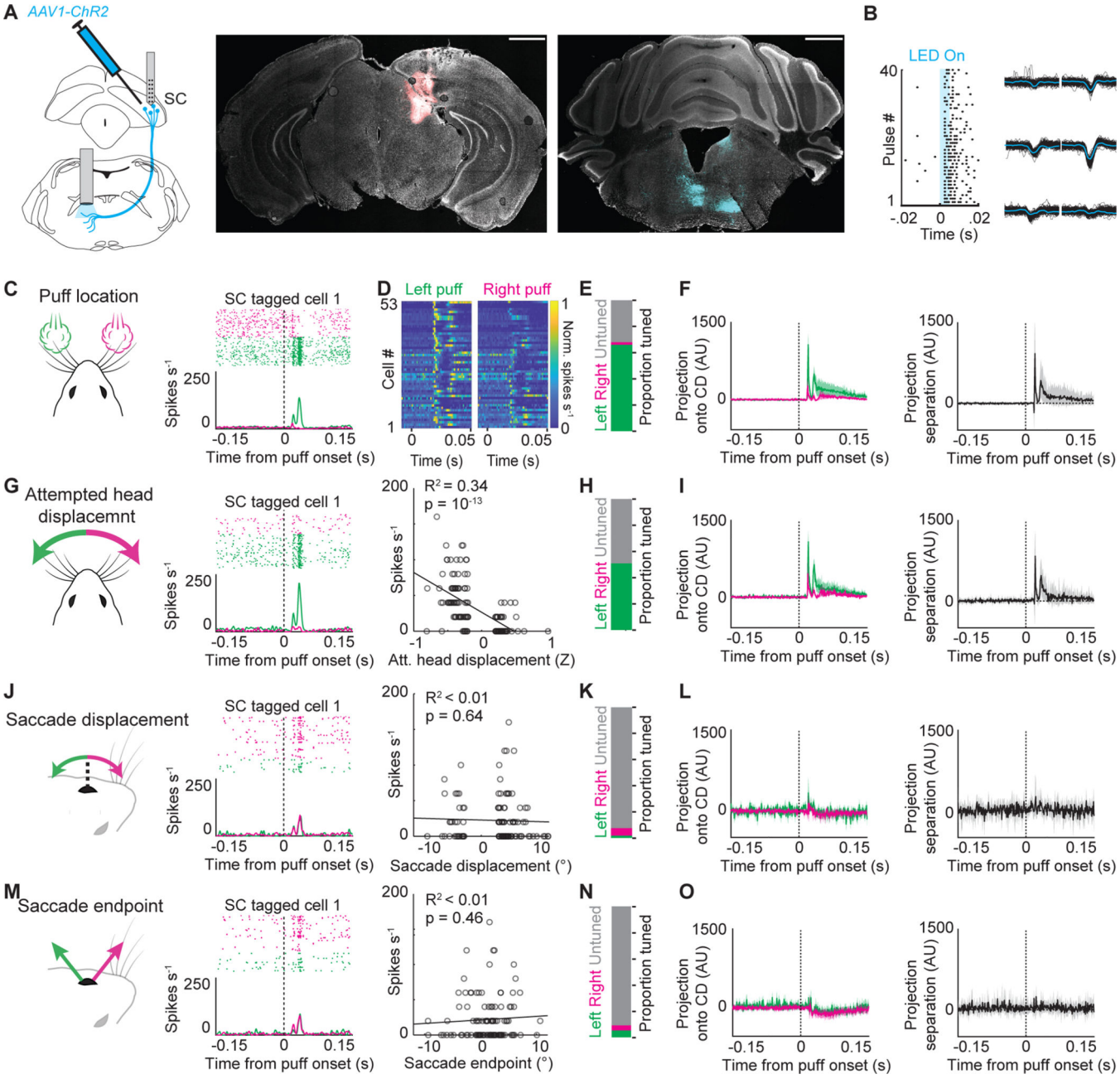

Figure 4. Tectoreticular neurons encode stimulus location and head displacement.

A, Left, schematic of antidromic "optotagging" of tectoreticular neurons. Middle, Sample SC histology. Right, sample PMRF histology. Scale bar, 1 mm. **B**, Example cell. Left, raster plots of activity aligned to LED onset. Right, waveforms of spontaneously occurring (black) and light-evoked (blue) action potentials. **C**, Left, schematic of airpuff delivery to whiskers. Right, spike rasters and peri-stimulus time histogram of activity of example cell aligned to airpuff onset sorted by airpuff location. **D**, Peak-normalized average firing rate of each tectoreticular cell aligned to airpuff onset. **E**, Proportion of cells significantly tuned for left or right airpuffs. **F**, Left, trial-averaged population activity projected onto the coding dimension (**CD**) for left and right whisker airpuffs. Right, separation between the left and

right whisker airpuff activity projections. **G**, Left, schematic of left and right attempted head displacements. Middle, spike raster and peri-stimulus time histogram of activity for example cell aligned to airpuff onset sorted by attempted head displacement direction. Right, single-trial analysis of the relationship between attempted head displacement and spiking in the 50 ms following airpuff onset for the same cell. **H**, Proportion of units significantly tuned for left and right head displacements. **I**, Left, trial-averaged population activity projected onto the coding dimension (**CD**) for left and right head displacements. Right, separation between the left and right head displacement activity projections. **J, M**, As in **G** for saccade displacements and saccade endpoints. **K, N**, As in **H** for saccade displacements and saccade endpoints. **L, O**, As in **I** for saccade displacements and saccade endpoints. Green and magenta denote left (contralateral to recording site) and right (ipsilateral to recording site) airpuff locations or movements. Left and right saccade endpoints were defined relative to the median eye position. Tuning for airpuffs was computed using Student's t-test ($p < 0.05$). Tuning for movement parameters was determined using linear regression ($p < 0.05$). The same example cell is shown in each panel. Shading denotes 99% confidence interval. Recordings were performed in 4 mice over 9 sessions, yielding 317 units of which 53 were identified as tectoreticular. See also Figures S3 **and** S4.

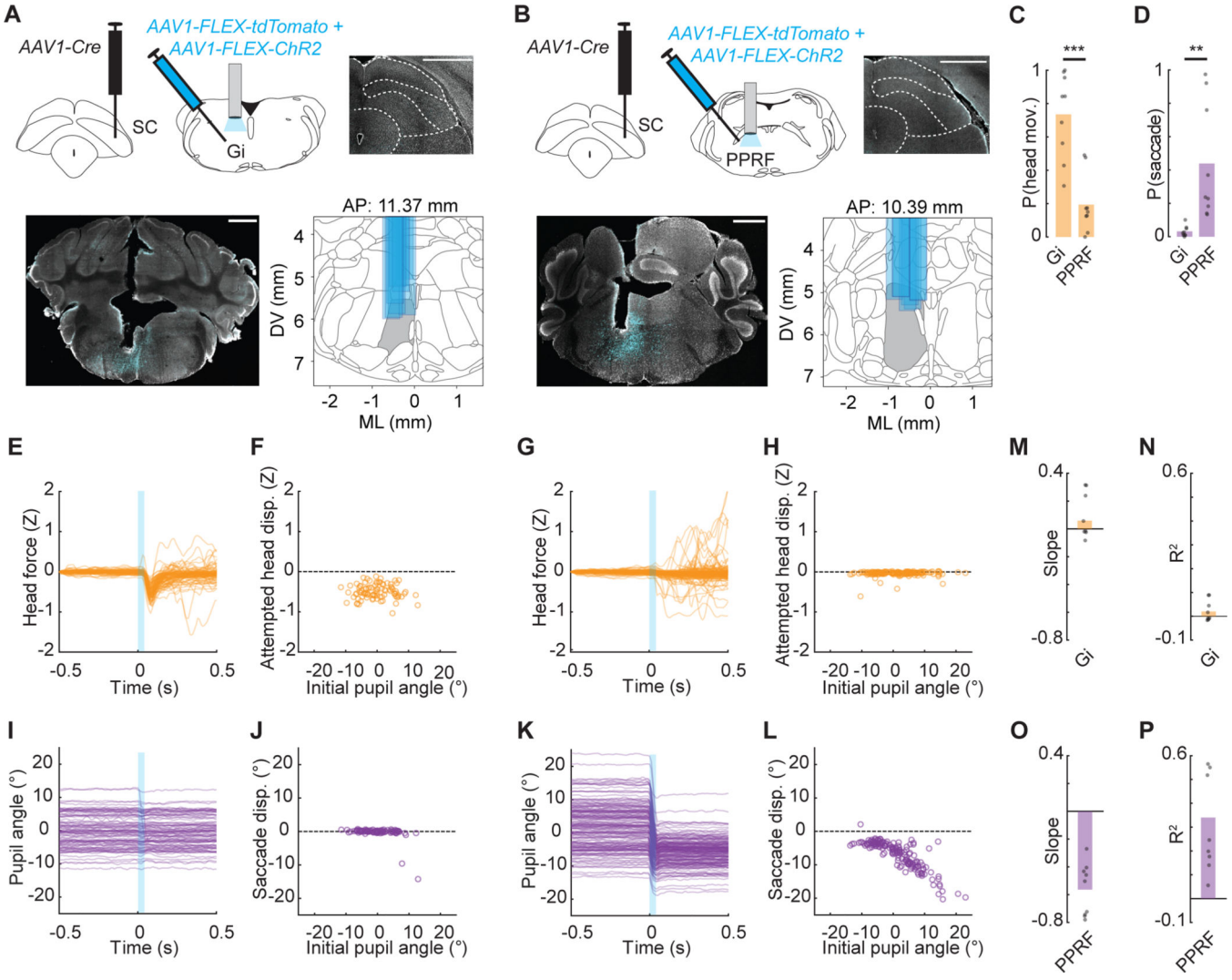

Figure 5. SC-recipient Gi and PPRF modules drive head movements with stereotyped displacements and saccades with stereotyped endpoints, respectively.

A, Top left, schematic. Top right, sample SC histology. Bottom left, sample Gi histology. Bottom right, fiber placements in Allen CCF. Scale bars, 1 mm. **B**, As in A but for SC-recipient PPRF neurons. **C, D**, Population summary of Gi and PPRF optogenetically evoked head movement (C) and saccade probability (**D**). **E**, Attempted head movements aligned to LED onset (blue shading) for sample Gi mouse. **F**, Relationship between initial pupil angle and head displacement for traces in **E. G, H**, as in **E, F** for sample PPRF mouse. **I**, Pupil traces aligned to LED onset (blue shading) for sample Gi mouse. **J**, Relationship between initial pupil angle and saccade displacement for traces in **I**. **K, L**, As in **I, J** but for SC-recipient PPRF neurons. Data in **E, F, I, J** derived from the same Gi stimulation animal. Data from **G, H, K, L** derived from the same PPRF stimulation animal. **M-O**, Population summary of slopes (M, O) and R^2 (N, P) for regression of Gi-evoked attempted head displacements (M, N) and PPRF-evoked saccade displacements (O, P) against initial pupil angle. Markers show individual animals (n = 9 for Gi, n = 9 for PPRF). Orange

denotes head data and purple denotes eye data. Statistics performed using Student's t-test (*$p < 0.05$; **$p < 0.01$; ***$p < 0.001$; ns, not significant).

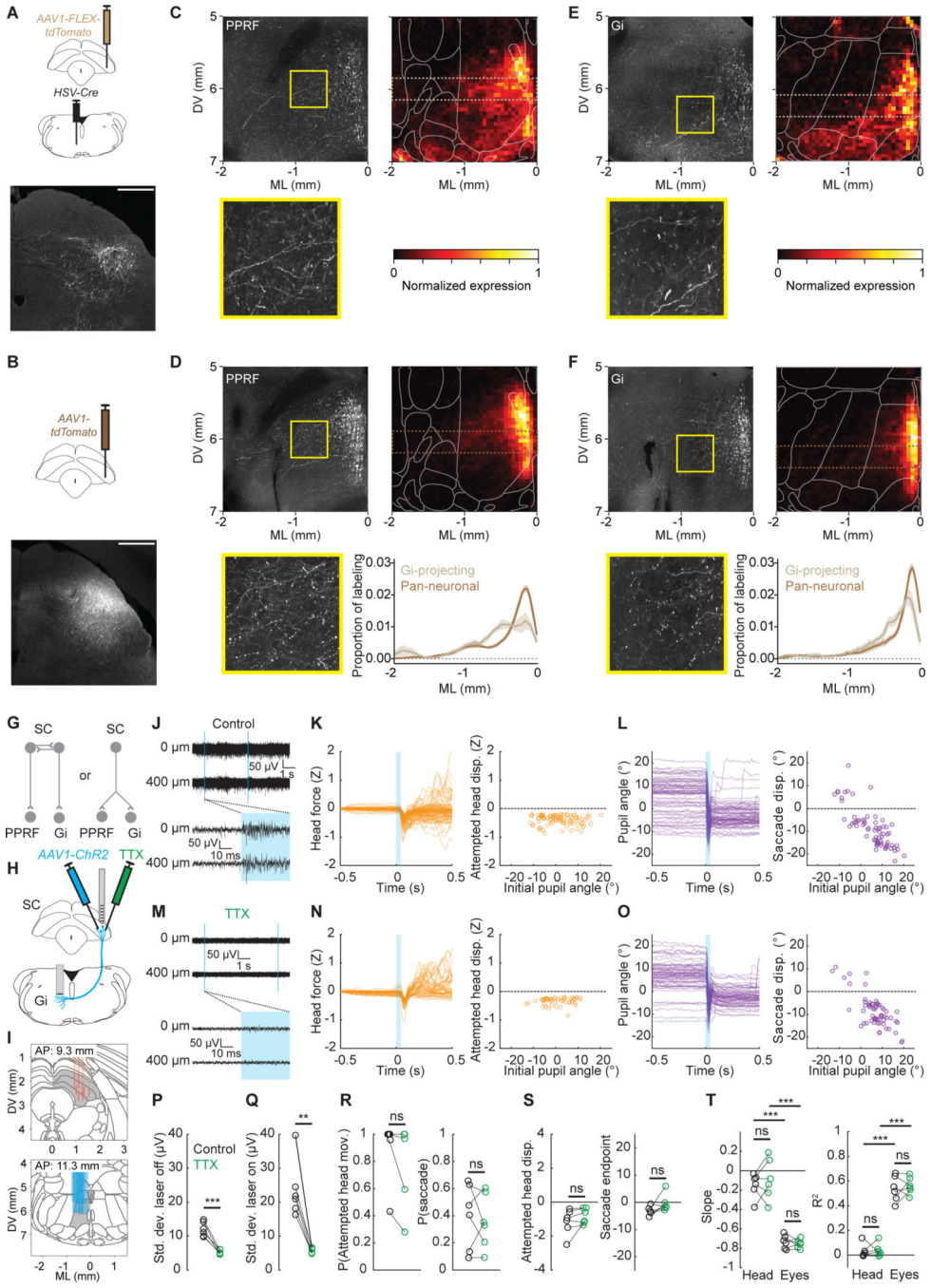

Figure 6. Individual tectoreticular neurons collateralizing to Gi and PPRF drive both head and eye movements.

A, Top, schematic of strategy to label Gi-projecting SC neurons (n = 3). Bottom, representative SC histology. Scale bar, 0.5 mm. **B**, As in **A** but for pan-neuronal SC labeling (n = 4). **C**, Gi-projecting neurons collateralize to PPRF. Top left, labeling in PPRF in representative animal. Yellow rectangle indicates area magnified at lower left. Top right, mean terminal density across animals. **D**, As in C for SC pan-neuronal labeling. Bottom right shows population mean distributions of terminals in PPRF in area outlined by dotted

lines in the mean terminal density images. **E, F**, As in **C, D** for terminals in Gi. **G**, Schematic of possible models. Left, model wherein separate SC neurons innervate PPRF and Gi to drive saccades and head movements, respectively. Right, model wherein single SC neurons collateralize to both PPRF and Gi to drive both head and eye movements. **H**, Schematic of approach. *AAV1-ChR2* was injected in right SC and a fiber optic was implanted over left Gi. SC was subsequently injected with either saline or TTX and SC activity was recorded. **I**, Positions of electrodes (top) and optical fibers (bottom) in Allen CCF. **J**, SC multiunit activity at 2 depths separated by 400 μm after control (saline) injection. **K**, Attempted head movements aligned to LED onset (blue shading) (left) and relationship between initial pupil angle and head displacement (right). **L**, as in **K** for saccades. **M**, TTX injection abolishes activity in SC. **N, O**, as in **K, L** after TTX injection in SC. Data in **J**-**L** and **M**-**O** are from the same mouse on successive days. **P**, Mean standard deviation of multiunit signals detected in SC for control and TTX sessions. Markers indicate single mice. **Q**, As in **P** for antidromically evoked SC activity. **R**, Probability of attempted head movements (left) and saccades (right) for control and TTX sessions. **S**, Size of attempted head movements (left) and saccade endpoints (right) for control and TTX sessions. **T**, Slopes (left) and R^2 (right) of regression of attempted head displacement and saccade displacement against initial eye position. Statistics performed using Student's t-test (*$p < 0.05$; **$p < 0.01$; ***$p < 0.001$; ns, not significant).

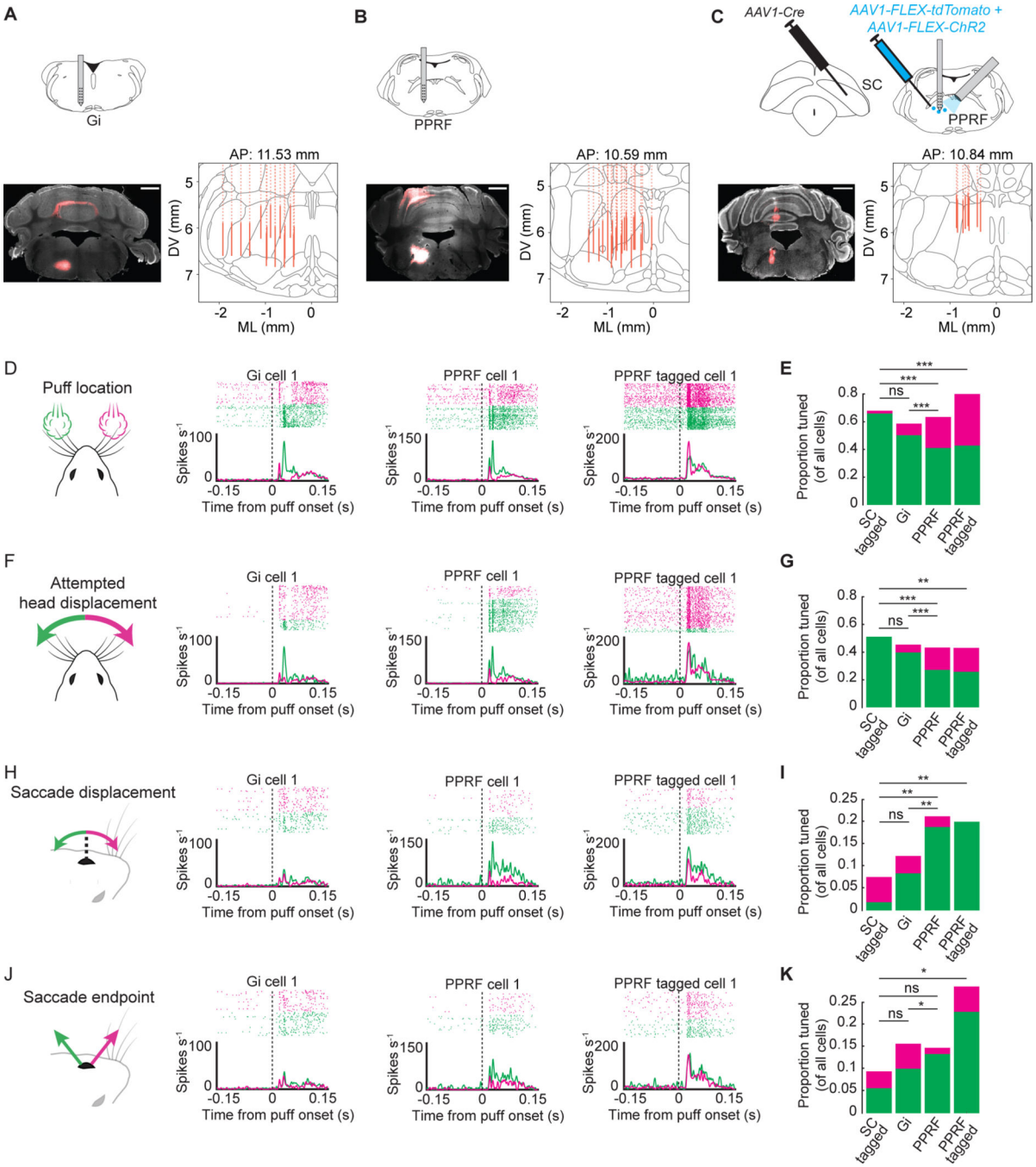

Figure 7. Saccade tuning emerges in PPRF.

A, B, C, Top, schematics of extracellular recordings of Gi (**A**), PPRF (**B**), and optotagged SC-recipient PPRF neurons (**C**). Bottom left, sample histology of recording site. Bottom right, recording sites in Allen CCF. **D**, Responses to left and right airpuffs for example Gi (left), PPRF (middle), and optotagged SC-recipient PPRF (right) neurons. **E**, Population summaries of airpuff tuning in optotagged SC tectoreticular, Gi, PPRF, and optotagged SC-recipient PPRF neurons. **F-K**, as in **D, E** but for attempted head displacement (**F, G**), saccade displacement (**H, I**), and saccade endpoint (**J, K**). Each row shows a single

example cell. Chi-squared tests were used to compare the proportions of left-, right-, and un-tuned units across structures (*p < 0.05; **p < 0.01; ***p < 0.001; ns, not significant). Gi recordings were performed in 4 mice over 6 sessions, yielding 179 cells. PPRF recordings were performed in 6 mice over 6 sessions, yielding 292 cells. Optotagged PPRF recordings were performed in 6 mice over 9 sessions, yielding 35 cells. SC recordings are from Figure 2. See also Figures S5, S6, and S7.

KEY RESOURCES TABLE

REAGENT or RESOURCE	SOURCE	IDENTIFIER
Virus strains		
AAV1-hSyn-ChR2(H134R)eYFP	Addgene	26973-AAV1
AAV1-EF1a-DIOhChR2(H134R)-eYFP	Addgene	20298-AAV1
AAV1-CAG-tdTomato	Addgene	59462-AAV1
AAV1-CAG-FLEX-tdTomato	Addgene	28306-AAV1
AAV1-hSyn-eGFP-Cre	Addgene	105540-AAV1
HSV-hEF1α-cre	MGH Gene Delivery Technology Core	RN425
AAV1-EF1a-DIO-eNpHR3.0eYFP	Addgene	26966-AAV1
Deposited data		
Primary data	This paper	10.5281/zenodo.7796128
Experimental models: Organisms/strains		
Adult male (8–12 weeks) C57BL/6J *mus musculus*	The Jackson Laboratory	000664
Software and algorithms		
Fiji	Fiji	https://fiji.sc
Kilosort v2.5	[87,88]	https://github.com/MouseLand/Kilosort/releases/tag/v2.5
Phy2	Cortex Lab	https://github.com/cortexlab/phy
RHX data acquisition software	Intan	https://intantech.com/RHX_software.html
Python 3.9	Python Software Foundation	https://www.python.org/downloads/
Matlab v2019a	Matlab	https://www.mathworks.com/products/matlab.html
DeepLabCut	[89]	http://www.mousemotorlab.org/deeplabcut
Allen CCF registration	[90]	https://github.com/cortexlab/allenCCF
3D rendering	[91]	https://github.com/brainglobe/brainrender
Custom analysis code	This paper	https://github.com/EvanFeinbergLab/Zahler_Taylor_2023
Other		
Laser scanning confocal microscope	Zeiss	LSM700
Stereotaxic Instrument	Kopf	Model 940 Small Animal
Micro syringe pump injector	World Precision Instruments	UMP3T-1
Ultraprecise micromanipulator	Sensapex	uMp micromanipulator system for electrophysiology
Tetrodotoxin citrate	Alomone Labs	T-550
DiI Stain	Thermofisher	D282
Optrode	Cambridge NeuroTech	ASSY-77 H6, 100 μm core lambda-b fiber with 300 μm horizontal separation between the probe and fiber
4-shank electrode	Neuronexus	A4×32-Poly2-5mm-23s-200177-AC128
Stimulating electrode	Neuronexus	A4×4-4mm-200-200-1250A16
Electrophysiology stimulation and recording system	Intan	RHS

REAGENT or RESOURCE	SOURCE	IDENTIFIER
473 nm fiber-coupled laser	Shanghai Laser & Optics Century	BL473T3-050FC + ADR700A
470 nm fiber-coupled LED	Thorlabs	M470F3
554 nm fiber-coupled LED	Thorlabs	MINTF4
Data acquisition device	NI	USB-6001
High speed camera	Flir	BFS-U3-28S5M-C
Miniature eye camera	Adafruit	1937
Load cell force sensor	Sparkfun	SEN-14727
Animal head tracking device (IMU)	Rosco	N/A
Cryostat	Cryostar	NX70
Ceramic ferrules	Thorlabs	CFLC440- 10
400 μm core 0.39 NA optical fiber	Thorlabs	FT400UMT
Low-autofluorescence epoxy	Eccobond	F112